CHANDRA X-RAY OBSERVATIONS OF THE 0.6 < z < 1.1 RED-SEQUENCE CLUSTER SURVEY SAMPLE

A. K. HICKS
Department of Astronomy, University of Virginia, Charlottesville, VA 22904; ahicks@alum.mit.edu

E. ELLINGSON
Center for Astrophysics and Space Astronomy, University of Colorado,
Boulder, CO 80309; elling@casa.colorado.edu

M. BAUTZ
MIT Kavli Institute for Astrophysics and Space Research, Cambridge, MA 02139; mwb@space.mit.edu

B. CAIN
MIT Kavli Institute for Astrophysics and Space Research, Cambridge, MA 02139; bcain@mit.edu

D. G. GILBANK
Department of Astronomy and Astrophysics, University of Toronto, Toronto,
ON M5S 3H4, Canada; dgilbank@astro.uwaterloo.ca

M. G. GLADDERS
Department of Astronomy and Astrophysics, University of Chicago,
Chicago, IL 60637; gladders@uchicago.edu

H. HOEKSTRA
Alfred P. Sloan Research Fellow, Department of Physics and Astronomy, University of Victoria,
Victoria, BC V8P 5C2, Canada; hoekstra@uvic.ca

H. K. C. YEE
Department of Astronomy and Astrophysics, University of Toronto, Toronto,
ON M5S 3H4, Canada; hyee@astro.utoronto.ca

AND

G. GARMIRE
Department of Astronomy and Astrophysics, Pennsylvania State University,
University Park, PA 16802; garmire@astro.psu.edu

ABSTRACT

We present the results of *Chandra* observations of 13 optically selected clusters with $0.6 < z < 1.1$, discovered via the Red-Sequence Cluster Survey (RCS). All but one are detected at $S/N > 3$, although three were not observed long enough to support detailed analysis. Surface brightness profiles are fitted to β models. Integrated spectra are extracted within R_{2500}, and T_X and L_X information is obtained. We derive gas masses and total masses within R_{2500} and R_{500}. Cosmologically corrected scaling relations are investigated, and we find the RCS clusters to be consistent with self-similar scaling expectations. However, discrepancies exist between the RCS sample and lower z X-ray–selected samples for relationships involving L_X, with the higher z RCS clusters having lower L_X for a given T_X. In addition, we find that gas mass fractions within R_{2500} for the high-z RCS sample are lower than expected by a factor of ~ 2. This suggests that the central entropy of these high-z objects has been elevated by processes such as preheating, mergers, and/or AGN outbursts, that their gas is still infalling, or that they contain comparatively more baryonic matter in the form of stars. Finally, relationships between red-sequence optical richness ($B_{\mathrm{gc,red}}$) and X-ray properties are fitted to the data. For systems with measured T_X, we find that optical richness correlates with both T_X and mass, having a scatter of $\sim 30\%$ with mass for both X-ray–selected and optically selected clusters. However, we also find that X-ray luminosity is not well correlated with richness and that several of our sample members appear to be significantly X-ray faint.

Subject headings: cosmology: observations — galaxies: clusters: general — X-rays: galaxies: clusters

Online material: color figures

1. INTRODUCTION

The Extended Medium Sensitivity Survey (EMSS; Gioia et al. 1990) sparked renewed interest in the ongoing search for clusters of galaxies at high redshift. Since then, numerous high-redshift surveys have been carried out, both optically (e.g., Gilbank et al. 2004; Donahue et al. 2002; Postman et al. 1996; Bower et al. 1994) and in the X-ray (e.g., Valtchanov et al. 2004; Bauer et al. 2002; Wilkes et al. 2000). The motivations for such searches are multi-faceted, but the most compelling of these are cosmological in nature.

Clusters of galaxies are an important source of information about the underlying cosmology of the universe. They are considered to be essentially "closed boxes," meaning that the primordial matter that they were initially assembled from has remained trapped in their deep potential wells since they were formed. This

makes them ideal objects with which to study galaxy formation and evolution. In addition, clusters are the largest virialized objects in the universe. By virtue of this fact we are able, through high-redshift samples, to investigate the growth of large-scale structure. A firm knowledge of the evolution of the cluster mass function would provide an enormous contribution to constraining cosmological parameters such as σ_8 (the normalization of the density perturbation spectrum) and w (the dark energy equation of state; e.g., Voit 2005).

Two ingredients are required to achieve this goal. First, a statistically significant sample of clusters in multiple redshift bins is needed. Second, reliable mass estimates of the clusters in that sample must be obtained. Difficulties in reaching the first requirement include the vast amount of telescope time required to carry out such a search in the X-ray and the propensity for false detections due to projection effects in optical surveys. The primary challenge in reaching the second part of this goal is again the high cost of observing time to achieve either X-ray or dynamical mass estimates.

The Red-Sequence Cluster Survey (RCS; Gladders & Yee 2000, 2005; Yee et al. 2007) has attempted to evade such difficulties: RCS is an optical survey that uses the color-magnitude relationship of cluster ellipticals to find galactic overdensities in small slices of redshift space. This technique has been estimated to bring false detection rates down to $\sim$5%–10% (Gladders 2002; Blindert et al. 2007; Cohn et al. 2007). The chosen filters (R_c and z') optimize this finding algorithm for the redshift range $0.2 < z < 1.2$ and provide photometric redshift information with accuracies of $\sim$10%. In addition, optical richness information is immediately available from the survey data, and, if sufficiently calibrated, this information could provide a highly efficient way to estimate the masses of cluster candidates.

The first phase of the Red-Sequence Cluster Survey (RCS-1; Gladders & Yee 2005), from which our cluster sample was drawn, covers 90 deg^2 and was performed at the Canada-France-Hawaii Telescope (CFHT) and the Cerro Tololo Inter-American Observatory (CTIO). RCS-1 has identified 6483 cluster candidates in the redshift range $0.2 < z < 1.2$, over 1000 of which are at least as optically rich as Abell class 0 clusters (Gladders & Yee 2005).

The motivations for this work are to characterize high-redshift optically selected cluster samples, probe cluster evolution, and move forward in attempts to calibrate a robust relationship between optical richness and cluster mass. This paper presents a detailed analysis of the *Chandra* data of 13 RCS-1 clusters with redshifts in the range $0.6 < z < 1.1$. Our analysis investigates the temperatures and gas distributions of 10 of these clusters and provides mass estimates for use in the calibration of relationships between optical richness and cluster mass.

We also use our results to investigate the X-ray scaling laws of our sample and thereby probe redshift evolution in these relationships. To facilitate comparisons between the RCS clusters and lower redshift X-ray–selected samples, we make use of our previous *Chandra* analysis of the Canadian Network for Observational Cosmology (CNOC) subsample of the EMSS (Hicks et al. 2006; Yee et al. 1996; Gioia et al. 1990). This sample, with redshifts in the range $0.1 < z < 0.6$, was chosen based on X-ray luminosity ($L_X \geq 2 \times 10^{44}$ ergs s^{-1}; Gioia et al. 1990).

This paper is organized as follows: In §§ 2 and 3 we introduce our sample and describe the basic properties of our data. In §§ 4 and 5 we investigate gas distributions and obtain cluster temperatures. We derive masses for our sample in § 6. High-z X-ray scaling relationships are examined in § 7, while correlations between optical richness and cluster X-ray properties are explored in § 8. In § 9 we investigate possible sources of bias in

cluster sample selection. A summary and discussion of our results are presented in § 10. Unless otherwise noted, this paper assumes a cosmology of $H_0 = 70$ km s^{-1} Mpc^{-1}, $\Omega_M = 0.3$, and $\Omega_\Lambda = 0.7$. All errors are quoted at 68% confidence levels.

2. CLUSTER SAMPLE AND OBSERVATIONS

Chandra Advanced CCD Imaging Spectrometer (ACIS) observations of 13 RCS clusters were taken during the period 2002 April 10–2005 October 23. Twelve of these clusters were observed with the ACIS-S CCD array, and one was observed with ACIS-I, with an overall range in individual exposures of 10–100 ks. Seven of the clusters in this sample were observed on multiple occasions. All multiple observations were merged for imaging analysis to provide higher overall signal-to-noise ratios (S/Ns). Those clusters with $\Delta t_{\rm obs} \leq 3$ months between observations were merged for spectral analysis as well. Each of the observations analyzed in this study possesses a focal plane temperature of -120°C.

Aspect solutions were examined for irregularities, and none were found. Background contamination due to charged particle flares was reduced by removing time intervals during which the background rate exceeded the average background rate by more than 20%. The quiescent background was further reduced by using VFAINT mode. The event files were then filtered on standard grades and bad pixels were removed. Table 1 provides a list of each of the clusters in our sample, including their precise designation (hereafter shortened for simplicity), redshift, ObsID, and corrected exposure information for each observation.

After the initial cleaning of each data set, 0.3–7.0 keV images, instrument maps, and exposure maps were created using the CIAO 3.3.0.1 tool MERGE_ALL. Data with energies below 0.3 keV and above 7.0 keV were excluded due to uncertainties in the ACIS calibration and background contamination, respectively. Ideally, all data below 0.6 keV would have been excluded to minimize low-energy uncertainties; however, the combined faintness and high redshifts of our objects require the utilization of lower energy photons as well. Point-source detection was performed by running the tools WTRANSFORM and WRECON on the flux images.

Figure 1 contains smoothed 0.3–7.0 keV *Chandra* flux images of each of the clusters in our sample (produced by the CIAO tool CSMOOTH), including a combined image of the three objects at $z \sim 0.9$ that belong to a supercluster in the 23$^{\rm h}$ field (Gilbank et al. 2008). As seen in the figure, this sample covers a wide range of cluster X-ray morphology, from very regular objects (e.g., RCS 1419+5326), through well-detected clusters with significant substructure (e.g., RCS 2318+0034), all the way to very disturbed systems (e.g., RCS 2112−6326). It is worth noting that in Figure 1 the brightest part of RCS 2318+0034 does not seem to lie at the center of the cluster, indicating that this object may have recently undergone a merger, or could at least possess an appreciable amount of substructure. Together, these clusters represent an assembly of some of the richest high-z ($0.6 < z < 1.1$) clusters in the RCS-1 survey.

3. SIGNAL-TO-NOISE RATIOS AND CLUSTER POSITIONS

To estimate the significance of RCS cluster detections in the X-ray, we made use of relatively simple statistics. Counts were extracted from a 500 h_{70}^{-1} kpc radius region around the aim point of each observation in the 0.3–7.0 keV band (C) and also from a region far away from the aim point on the same chip that served as a background (B). Obvious point sources were removed from each region. S/Ns were calculated based on dividing net counts, $N = C - B$, by the standard deviation, $\sigma = (C + B)^{1/2}$. Using

TABLE 1

Cluster Sample

Cluster	z	$1''$ (h_{70}^{-1} kpc)	ObsID	Individual Exposure (s)	Total Exposure (s)
RCS 022434−0002.5..................	0.778[a]	7.44	3181	12051	100844
	0.778[a]	7.44	4987	88793	100844
RCS 043938−2904.7..................	0.960[b]	7.93	3577	64507	93263
	0.960[b]	7.93	4438	28756	93263
RCS 110723−0523.3..................	0.735[c]	7.28	5825	49466	94058
	0.735[c]	7.28	5887	44592	94058
RCS 132631+2903.1	0.75[d]	7.34	3291	30907	65499
	0.75[d]	7.34	4362	34592	65499
RCS 141658+5305.2	0.968[c]	7.95	3239[e]	62824	62824
RCS 141910+5326.2	0.62[f]	6.79	3240	9904	57307
	0.62[f]	6.79	5886	47403	57307
RCS 162009+2929.4	0.870[c]	7.71	3241	35953	35953
RCS 211223−6326.0..................	1.099[g]	8.17	5885	70520	70520
RCS 215641−0448.1..................	1.080[g,h]	8.14	5353	36558	71259
	1.080[g,h]	8.14	5359	34701	71259
RCS 231831+0034.2	0.78[f]	7.44	4938	50454	50454
RCS 231953+0038.0	0.900[i]	7.79	5750	20902	74539
(RCS 231948+0030.1)	(0.904)[i]	(7.80)	7172	17947	74539
(RCS 232002+0033.4)	(0.901)[i]	(7.79)	7173	20899	74539
	(0.901)[i]	(7.79)	7174	14791	74539

[a] Hicks et al. (2007).
[b] Cain et al. (2008).
[c] Gilbank et al. (2007).
[d] From photometric data (Gladders & Yee 2005). This cluster may be at $z \sim 1.01$ (see text for explanation).
[e] ACIS-I observation.
[f] From X-ray spectra (this work); see text.
[g] L. F. Barrientos et al. (2008, in preparation).
[h] ID uncertain (see L. F. Barrientos et al. 2008, in preparation).
[i] Gilbank et al. (2008).

this method, 12 cluster signals were detected at an S/N greater than 3, with the remaining object detected at S/N = 1.1 (Table 2).

Using adaptively smoothed 0.3–7.0 keV flux images (Fig. 1), we determined the location of the X-ray emission peak of each cluster. The images of RCS 2112−6326 and RCS 2156−0448 appear to contain multiple regions of extended emission; therefore, we cannot determine a precise X-ray position for these objects. In the case of RCS 1326+2903, two RCS 13$^{\rm h}$ clusters lie in the field of view. The original observation was designed to observe a $z = 1.01$ cluster at R.A. = 13$^{\rm h}$26$^{\rm m}$29$^{\rm s}$, decl. = +29°03′06″ (J2000.0). Our astrometry indicates, however, that we are most likely detecting the emission of a lower redshift RCS cluster ($z = 0.75$) at an optical position of R.A. = 13$^{\rm h}$26$^{\rm m}$31$^{\rm s}$, decl. = +29°03′12″. Because of the uncertainty surrounding this detection, we have carried both possibilities throughout much of our analysis; however, we include the more likely candidate (at $z = 0.75$) in our subsequent fitting and plots. All other clusters (with the exceptions of RCS 2112−6326 and RCS 2156−0448) were found within 31″ of their optical positions. Table 2 lists optical positions, X-ray positions, net counts within 500 h_{70}^{-1} kpc, and S/Ns derived from the method described above.

4. SURFACE BRIGHTNESS

A radial surface brightness profile was computed over the range 0.3–7.0 keV in circular annuli for each cluster. These profiles were then fitted with β models:

$$I(r) = I_B + I_0 \left(1 + \frac{r^2}{r_c^2} \right)^{-3\beta + 1/2}, \qquad (1)$$

where I_B is a constant representing the surface brightness contribution of the background, I_0 is the normalization, and r_c is the core radius. Fits were performed to just past the radii at which the cluster's surface brightness met the background (usually ~200″). The parameters of the best-fitting models of the 10 clusters for which surface brightness fitting was possible are shown in Table 3, and images of these fits are given in Figure 2. Although many of the clusters exhibit hints of substructure, most were reasonably well fitted by a β model (see Table 3 for goodness-of-fit data). Other than somewhat low normalizations, the results of surface brightness fitting are unremarkable ($0.51 < \beta < 0.72$), except in the two cases of RCS 1326+2903 ($\beta = 1.04$), which lies at the edge of our detection threshold (Table 2), and RCS 2318+0034, which appears to not be completely relaxed, as its brightest emission is slightly offset from the center of its extended emission (Fig. 1).

5. SPECTRAL ANALYSIS

5.1. Integrated Spectral Fits and R_{2500}

Spectra were extracted from each point-source–removed event file in a circular region with a 300 h_{70}^{-1} kpc radius. In the cases of RCS 0224−0002 and RCS 1419+5326 ($\Delta t_{\rm obs} > 2$ yr), individual spectra were extracted from each ObsID and fitted simultaneously. The spectra were analyzed with XSPEC (Arnaud 1996), using weighted response matrices (RMFs) and effective area files (ARFs) generated with the CIAO tool SPECEXTRACT and CALDB 3.2.2. Background spectra were extracted from the aimpoint chip as far away from the aim point as possible.

Spectra were fitted with single-temperature spectral models, inclusive of foreground absorption. Each spectrum was fitted with the absorbing column frozen at its measured value (Dickey &
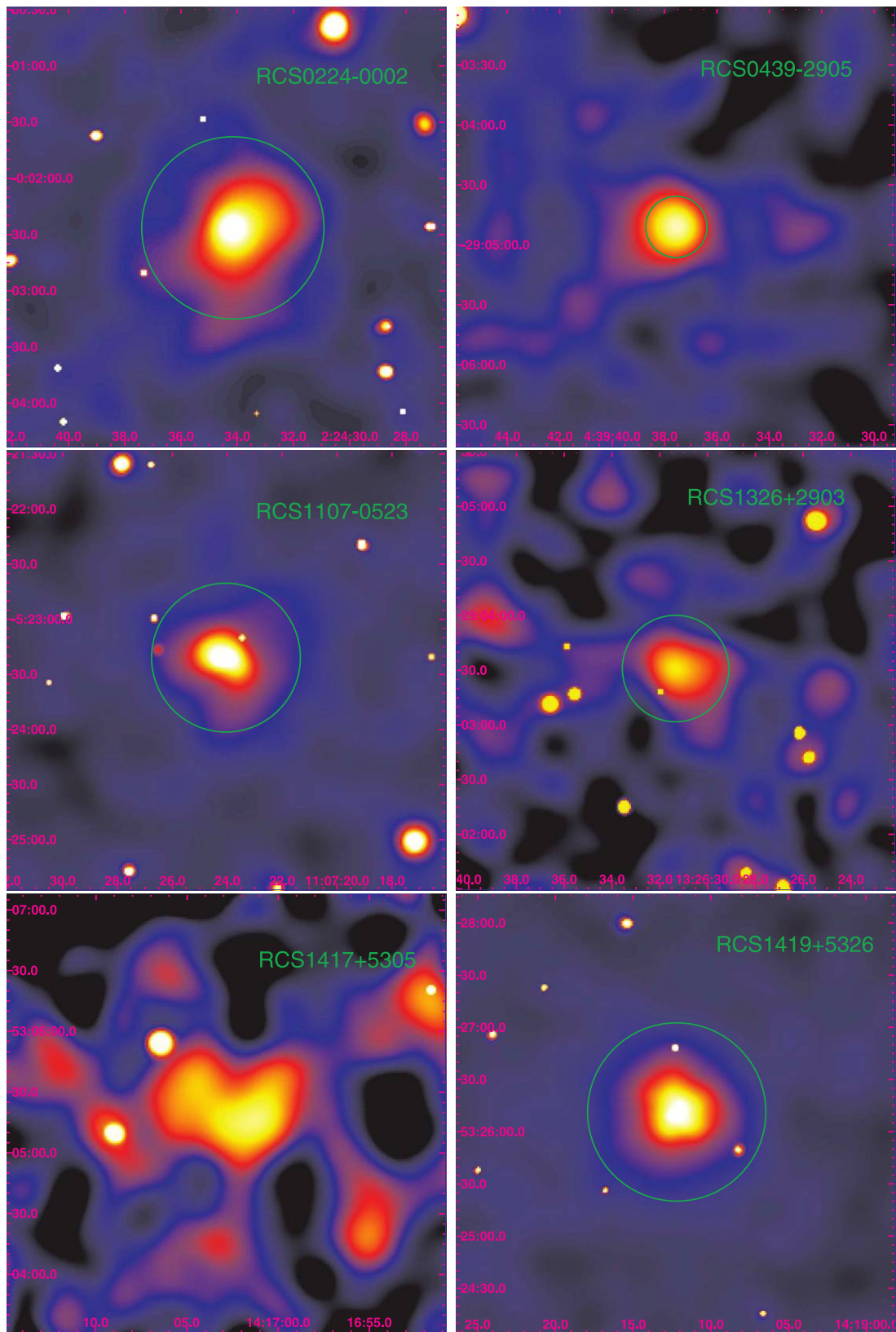
Fig. 1.—Adaptively smoothed X-ray flux images of our sample in the 0.3−7.0 keV band. Circles denote calculated values of R_{2500} for each cluster. The three single cluster images that lack circles did not contain enough cluster signal to constrain a β model or a temperature and thus lack estimates of R_{2500}. In each image, north is up and east is to the left. The last image shows the three clusters that make up the $z = 0.9$ supercluster in the 23^h field. The aim-point cluster (RCS 2319+0038) lies at the top of the image on the back-side−illuminated CCD ACIS-S3, and the other two clusters (RCS 2319+0030 and RCS 2320+0033) lie on the front-side−illuminated CCD ACIS-S2. Instrumental differences in the two chips cause their respective backgrounds to have slightly different values in the image.
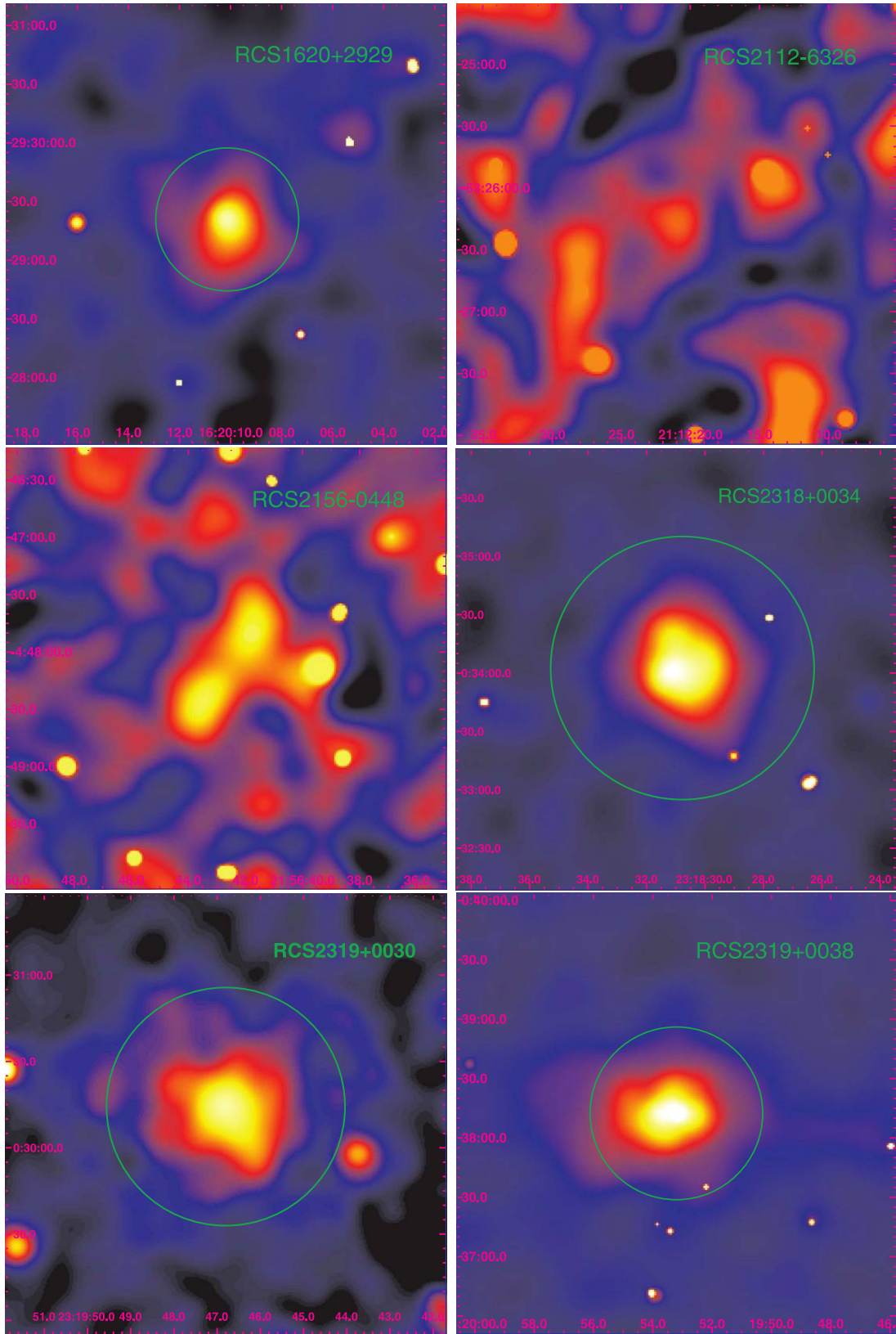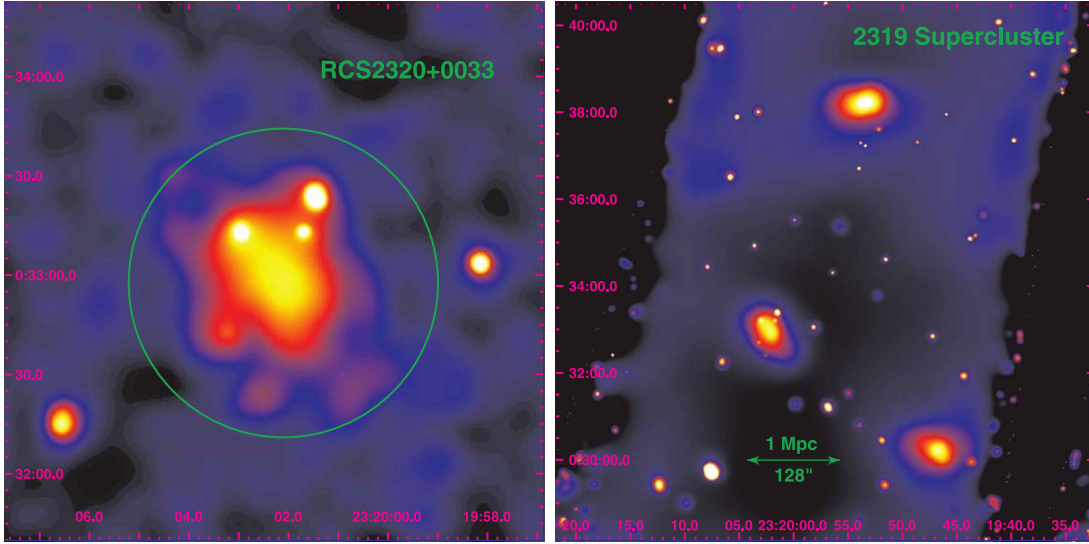
Fig. 1—*Continued*

Fig. 1—*Continued*

TABLE 2
CLUSTER POSITIONS AND DETECTION DETAILS

	OPTICAL POSITION[a]		X-RAY POSITION[a]		SEPARATION		
CLUSTER	R.A.	Decl.	R.A.	Decl.	(arcsec)	NET COUNTS[b]	S/N
RCS 0224−0002............................	02 24 34.1	−00 02 30.9	02 24 34.2	−00 02 26.4	4.7	1102	16.2
RCS 0439−2904............................	04 39 38.0	−29 04 55.2	04 39 37.6	−29 04 50.3	7.2	461	6.5
RCS 1107−0523............................	11 07 23.4	−05 23 13.7	11 07 24.0	−05 23 20.7	11.4	1056	15.5
RCS 1326+2903[c]........................	13 26 31	+29 03 12	13 26 31.3	+29 03 31.0	19.9	181	3.1
RCS 1417+5305	14 16 59.8	+53 05 12.2	14 17 01.5	+53 05 16.2	15.8	138	4.7
RCS 1419+5326	14 19 12.1	+53 26 11.0	14 19 12.1	+53 26 11.6	0.6	2903	40.2
RCS 1620+2929	16 20 10.0	+29 29 21.5	16 20 10.1	+29 29 20.8	1.5	257	7.1
RCS 2112−6326............................	21 12 23.1	−63 25 59.5	. . .	. . .	. . .	232	4.8
RCS 2156−0448............................	21 56 41.2	−04 48 13.3	. . .	. . .	. . .	54	1.1
RCS 2318+0034	23 18 31.5	+00 34 18.0	23 18 30.8	+00 34 02.5	19.9	1161	21.5
RCS 2319+0030	23 19 48.7	+00 30 08.5	23 19 46.8	+00 30 14.3	29.1	780	17.8
RCS 2319+0038	23 19 53.9	+00 38 11.6	23 19 53.2	+00 38 12.5	10.5	1742	26.2
RCS 2320+0033	23 20 03.0	+00 33 25.1	23 20 02.1	+00 32 57.6	30.6	725	16.8

NOTE.—Units of right ascension are hours, minutes, and seconds, and units of declination are degrees, arcminutes, and arcseconds.
[a] All positions are given for equinox J2000.0.
[b] The 0.3–7.0 keV band, within $R < 500\ h_{70}^{-1}$ kpc.
[c] There is also an RCS cluster at $13^h26^m29^s$, $+29°03'06''$, which is 39.2″ from the X-ray centroid (see text for details).

TABLE 3
β MODEL FITS

Cluster	r_c (h_{70}^{-1} kpc)	β	I_0[a]	I_B[a]	χ^2/dof
RCS 0224−0002........................	180^{+13}_{-12}	$0.72^{+0.04}_{-0.04}$	$7.1^{+0.4}_{-0.4}$	$2.33^{+0.02}_{-0.02}$	210.7/199
RCS 0439−2904........................	108^{+8}_{-7}	$0.59^{+0.04}_{-0.04}$	$5.2^{+0.4}_{-0.3}$	$3.80^{+0.03}_{-0.04}$	67.8/64
RCS 1107−0523........................	31^{+2}_{-2}	$0.51^{+0.01}_{-0.01}$	62^{+5}_{-4}	$2.5^{+0.1}_{-0.1}$	216.1/191
RCS 1326+2903	148^{+11}_{-9}	$1.04^{+0.08}_{-0.06}$	$3.4^{+0.3}_{-0.2}$	$2.97^{+0.03}_{-0.03}$	54.9/64
RCS 1419+5326	52^{+2}_{-2}	$0.60^{+0.01}_{-0.01}$	189^{+9}_{-7}	$2.34^{+0.02}_{-0.02}$	170.6/155
RCS 1620+2929	85^{+14}_{-12}	$0.60^{+0.05}_{-0.04}$	13.3^{+1}_{-1}	$1.98^{+0.04}_{-0.04}$	147.7/148
RCS 2318+0034	171^{+7}_{-4}	$0.86^{+0.04}_{-0.02}$	29^{+1}_{-1}	$2.56^{+0.02}_{-0.02}$	304.8/300
RCS 2319+0030	113^{+8}_{-7}	$0.54^{+0.03}_{-0.02}$	$19.7^{+1.5}_{-0.7}$	$1.86^{+0.03}_{-0.02}$	209.2/155
RCS 2319+0038	100^{+7}_{-6}	$0.65^{+0.03}_{-0.02}$	46^{+3}_{-2}	$2.61^{+0.02}_{-0.02}$	153.6/155
RCS 2320+0033	117^{+8}_{-8}	$0.61^{+0.03}_{-0.02}$	$18.9^{+1.0}_{-1.0}$	$1.74^{+0.03}_{-0.03}$	162.8/147

[a] Surface brightness I in units of 10^{-9} photons s^{-1} cm^{-2} arcsec^{-2}.
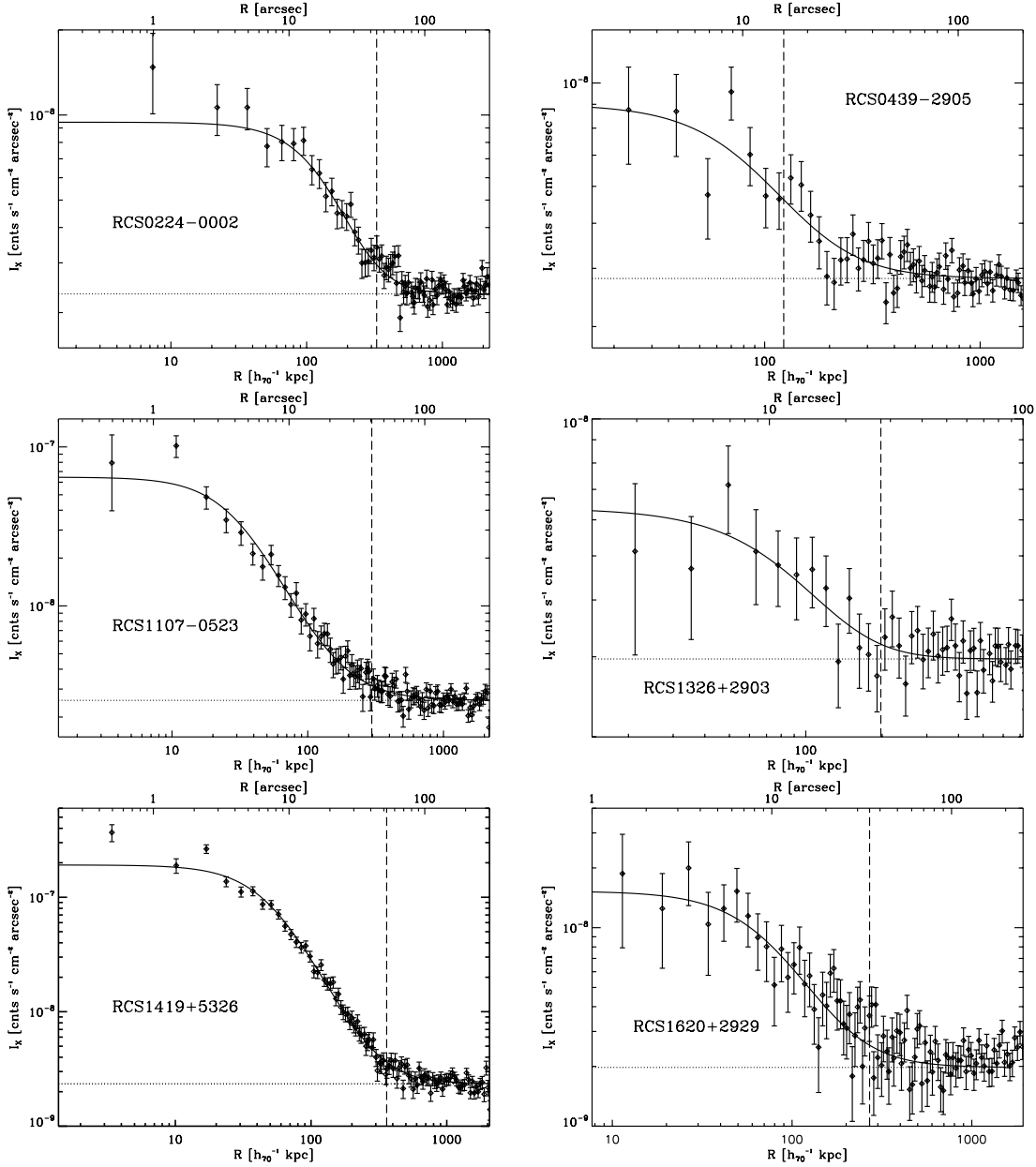
FIG. 2.—Radial surface brightness profiles for the 0.3–7.0 keV band accumulated in annular bins for 10 clusters in our sample. A solid line traces the best-fitting β model of each cluster. Horizontal dotted lines represent best-fit background values, and vertical dashed lines indicate R_{2500}. Many of the profiles exhibit some substructure; however, most were reasonably well fitted by a standard β model (see Table 3 for goodness-of-fit data).

Lockman 1990). Metal abundances were initially fixed at a value of 0.3 solar (Edge & Stewart 1991). Data with energies below 0.3 keV and above 7.0 keV were excluded from the fits.

Three of the clusters did not possess enough counts to constrain a spectral fit. The results of the 10 successful fits, combined with best-fitting β model parameters from § 4, were then used to estimate the value of R_{2500} for each cluster. This is accomplished by combining the equation for total gravitating mass (Sarazin 1988)

$$M_{\text{tot}}(<r) = -\frac{kT(r)r}{G\mu m_p}\left(\frac{\partial \ln \rho}{\partial \ln r} + \frac{\partial \ln T}{\partial \ln r}\right) \qquad (2)$$

(where μm_p is the mean mass per particle) with the definition of mass overdensity

$$M_{\text{tot}}(r_\Delta) = \frac{4}{3}\pi\rho_c(z)r_\Delta^3\Delta, \qquad (3)$$

where z is the cluster redshift and Δ is the factor by which the density at r_Δ exceeds $\rho_c(z)$, the critical density at z. Here $\rho_c(z)$ is given by $\rho_c(z) = 3H(z)^2/8\pi G = 3H_0^2 E_z^2/8\pi G$, where $E_z = [\Omega_m(1+z)^3 + \Omega_\Lambda]^{1/2}$. These equations are then combined with the density profile implied from the β model (assuming hydrostatic equilibrium, spherical symmetry, and isothermality)

$$\rho_{\text{gas}}(r) = \rho_0\left(1 + \frac{r^2}{r_c^2}\right)^{-3\beta/2}, \qquad (4)$$

resulting in the equation

$$\frac{r_\Delta}{r_c} = \sqrt{\left[\frac{3\beta kT}{G\mu m_p(4/3)\pi\rho_c(z)r_c^2\Delta}\right] - 1} \qquad (5)$$
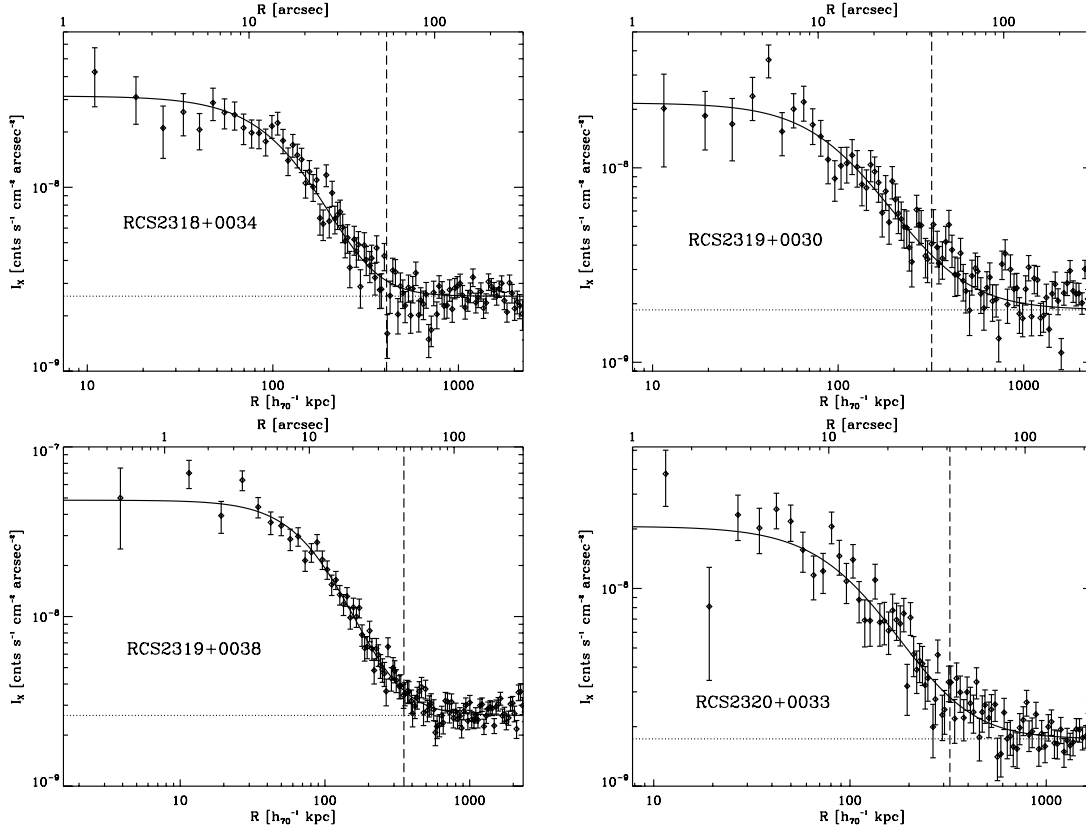
(Ettori 2000; Ettori et al. 2004b).

Fig. 2—*Continued*

After the initial estimation of R_{2500}, additional spectra were extracted from within that radius, and spectral fitting was performed again. This procedure was repeated until temperatures and values of R_{2500} were consistent for a given spectrum. Where statistically possible, additional fits were performed allowing abundances to vary also. Redshifts were also fitted (allowing only z, T_X, and normalization to vary) for the three clusters in our sample that do not have spectroscopic redshifts. We were unable to constrain a redshift for RCS 1326+2903. The fits of the other two clusters resulted in $z = 0.62 \pm 0.01$ for RCS 1419+5326 and $z = 0.78^{+0.07}_{-0.08}$ for RCS 2318+0034, within 10% and 14%, respectively, of photometric redshift estimates obtained using the color of the red sequence (Gladders & Yee 2005). Fits with redshift fixed at these values were used in subsequent analysis (Table 4). The small uncertainties in these values ($\leq 10\%$) do not substantially affect our analysis.

Unabsorbed 2–10 keV luminosities within R_{2500} were calculated using fixed abundance fits. These were then converted to bolometric luminosities by scaling, using a thermal emission model in PIMMS. For the three clusters for which spectral temperature fitting was impossible (RCS 1417+5305, RCS 2112−6326, and RCS 2157−0448), spectra were extracted within 500 h_{70}^{-1} kpc radii and fitted in XSPEC with temperatures fixed at 4 keV (slightly lower than the average T_X of the sample) to determine their luminosities. Temperature uncertainties of ±2 keV were folded into the errors of these estimates. To estimate $L_X(\Delta = 500)$, we extracted spectra from within that radius for the 10 clusters in our detailed analysis sample and again used fixed abundance fits, with temperatures also fixed at the R_{2500} value. The results of spectral fitting are shown in Table 4, along with 68% confidence ranges. Bolometric X-ray luminosities are listed with richness measurements in Table 5.

5.2. T_X-σ Comparisons

Velocity dispersions for three of the clusters in this sample were obtained from Gilbank et al. (2007, 2008) and are listed in Table 6. Using the σ-T_X relationship of Xue & Wu (2000), $\sigma = 10^{2.49} T_X^{0.65}$, we find that our temperatures are in agreement with the clusters' measured velocity dispersions in all cases (Table 6). This result indicates that these three systems, at least, are not overly disturbed.

6. MASS ESTIMATES

An isothermal cluster whose surface brightness is well fitted by a β model can be shown to have a gas density profile that follows equation (4). Using this relationship and the equation of hydrostatic equilibrium (eq. [2]), total mass can be determined via

$$M_{\text{tot}}(<r) = \frac{3\beta}{G} \frac{kTr}{\mu m_p} \frac{(r/r_c)^2}{1 + (r/r_c)^2}. \tag{6}$$

To estimate gas mass (again assuming hydrostatic equilibrium, isothermality, and sphericity), the first step is to obtain a central density ($n_0 \equiv \rho_0/m_p$). There are two complementary ways to go about this. One is to use the surface brightness normalization:

$$n_0 = \left\{ \frac{\Gamma(3\beta)}{\pi^{1/2}\Gamma(3\beta - 1/2)} \left(\frac{\mu_e}{X_H \epsilon_0}\right) \left[\frac{I_0}{r_c(1+z)^4}\right] \right\}^{1/2}, \tag{7}$$

where the Γ function results from surface brightness integration, β comes from the fit to surface brightness, μ_e is the mean atomic mass per free electron (0.62), X_H is the hydrogen mass fraction

TABLE 4
INTEGRATED SPECTRAL FITS ($\Delta = 2500$)

Cluster	R_{2500} (h_{70}^{-1} kpc)	kT (keV)	Z ($Z_\odot$)	N_H (10^{20} cm^{-2})	χ^2/dof
RCS 0224−0002...................................	329^{+52}_{-35}	$5.0^{+1.2}_{-0.8}$	0.3	2.91	48.7/65
...	...	$5.1^{+1.2}_{-0.9}$	$0.2^{+0.4}_{-0.2}$	2.91	48.7/64
RCS 0439−2904...................................	123^{+24}_{-17}	$1.5^{+0.3}_{-0.2}$	0.3	2.63	8.0/10
RCS 1107−0523...................................	296^{+29}_{-22}	$4.2^{+0.8}_{-0.6}$	0.3	4.24	52.2/61
...	...	$4.2^{+0.6}_{-0.5}$	$0.7^{+0.5}_{-0.3}$	4.24	50.1/60
RCS 1326+2903	202^{+65}_{-34}	$1.5^{+0.6}_{-0.3}$	0.3	1.16	9.3/11
RCS 1326+2903 ($z = 1.01$)....................	128^{+79}_{-37}	$1.6^{+0.7}_{-0.3}$	0.3	1.16	8.9/11
RCS 1419+5326	356^{+17}_{-13}	$4.5^{+0.4}_{-0.3}$	0.3	1.18	126.3/125
...	...	$4.6^{+0.4}_{-0.3}$	$0.3^{+0.1}_{-0.1}$	1.18	126.2/124
RCS 1620+2929	270^{+53}_{-34}	$3.9^{+1.3}_{-0.9}$	0.3	2.72	14.1/20
...	...	$3.9^{+1.2}_{-0.8}$	$0.3^{+0.8}_{-0.3}$	2.72	14.1/19
RCS 2318+0034	410^{+49}_{-37}	$6.1^{+1.3}_{-0.9}$	0.3	4.13	48.9/68
...	...	$5.8^{+1.2}_{-0.8}$	$0.6^{+0.3}_{-0.3}$	4.13	47.4/67
RCS 2319+0030	319^{+55}_{-28}	6.5^{+1}_{-1}	0.3	4.13	44.8/34
...	...	6^{+1}_{-1}	$0.6^{+0.4}_{-0.4}$	4.13	44.3/33
RCS 2319+0038	351^{+29}_{-25}	$6.2^{+0.9}_{-0.8}$	0.3	4.16	72.4/81
...	...	$5.9^{+0.8}_{-0.7}$	$0.5^{+0.2}_{-0.2}$	4.16	70.9/80
RCS 2320+0033	323^{+53}_{-34}	5.9^{+2}_{-1}	0.3	4.14	31.2/32
...	...	6.0^{+2}_{-1}	$0.3^{+0.4}_{-0.3}$	4.14	31.1/31

NOTES.—Single-temperature fits within R_{2500}. When possible, a second fit was performed allowing both the temperature and abundance to vary. These fits are reported in the second line (where there is one) for each cluster. In the case of RCS 1326+2903, the second line indicates the result of fitting the integrated spectrum with a fixed abundance and a redshift of $z = 1.01$.

(0.707), ϵ_0 is the gas emissivity, I_0 is the best-fitting surface brightness normalization (corrected for absorption), and r_c is the core radius.

A second method of estimating central density makes use of both imaging and spectral fitting:

$$n_0^2 = \frac{4\pi d_{\mathrm{ang}}^2 (1+z)^2 K \times 10^{14}}{0.82(4\pi) r_c^3 \mathrm{EI}} \ \ \mathrm{cm}^{-6}. \qquad (8)$$

Here K is the normalization of the XSPEC model and EI is the emission integral, estimated by integrating the (spherical) emission from the source out to some radius: in our case we use 10 Mpc following the method of Ettori et al. (2003).

For the RCS sample we employed both of these methods, as it was crucial to confirm that we were not underestimating central density in these comparatively low luminosity objects. We also added the data from our previous Chandra analysis of the moderate-redshift CNOC sample, to cover a wider range of redshifts in our comparison. We found that the methods agree (on average) to within 10% and proceeded in our analysis using the surface brightness normalization method.

From these equations, along with equations (4) and (5), and using the results of spectral and surface brightness fitting, gas masses and total masses were determined out to R_{2500} and R_{500} for the clusters in this sample. We also calculate core gas mass fractions (within R_{2500} and R_{500}) for the RCS clusters and find them to be systematically lower than the core gas mass fractions of lower

TABLE 5
CLUSTER RICHNESS AND LUMINOSITY

Cluster	$B_{\mathrm{gc,red}}$ (h_{50}^{-1} Mpc$^{1.77}$)	$L_X(R_{2500})$ (10^{44} ergs s^{-1})	$L_X(R_{500})$ (10^{44} ergs s^{-1})
RCS 0224−0002...............................	945 ± 210	$2.1^{+0.3}_{0.2}$	$4.4^{+0.5}_{0.5}$
RCS 0439−2904...............................	1590 ± 460	$1.5^{+0.5}_{0.5}$	$4.0^{+0.7}_{0.8}$
RCS 1107−0523...............................	899 ± 280	$2.3^{+0.3}_{0.2}$	$3.5^{+0.3}_{0.4}$
RCS 1326+2903	381 ± 275	$0.4^{+0.3}_{0.3}$	$1.1^{+0.5}_{0.5}$
RCS 1326+2903 ($z = 1.01$)..............	2670 ± 671	$1.1^{+0.7}_{0.5}$	$2.7^{+1.0}_{1.0}$
RCS 1417+5305	1879 ± 464	$1.3^{+0.9}_{2.0}$[a]	...
RCS 1419+5326	1173 ± 224	$7.0^{+0.4}_{0.3}$	$8.4^{+0.5}_{0.5}$
RCS 1620+2929	906 ± 236	$2.3^{+0.7}_{0.3}$	$3.3^{+0.5}_{0.7}$
RCS 2112−6326...............................	1011 ± 400	$1.2^{+0.8}_{2.5}$[a]	...
RCS 2156−0448...............................	481 ± 166	$0.1^{+0.1}_{0.3}$[a,b]	...
RCS 2318+0034	996 ± 217	$6.0^{+0.7}_{0.4}$	$8.3^{+0.9}_{0.7}$
RCS 2319+0030	1150 ± 281	$3.6^{+0.6}_{0.4}$	$7.9^{+0.7}_{0.8}$
RCS 2319+0038	1515 ± 323	$7.6^{+0.6}_{0.4}$	$16.2^{+0.6}_{0.8}$
RCS 2320+0033	578 ± 202	$4.2^{+0.5}_{0.3}$	$5.9^{+0.5}_{0.6}$

[a] Bolometric X-ray luminosity within 500 h_{70}^{-1} kpc, assuming a temperature of 4 keV.
[b] ID uncertain (L. F. Barrientos et al. 2008, in preparation).

TABLE 6
DYNAMICAL COMPARISONS

Cluster	σ (km s^{-1})	$10^{2.49}T_X^{0.65}$[a] (km s^{-1})
RCS 1107−0523..................	700 ± 300	785^{+95}_{-74}
RCS 1620+2929	1050 ± 340	748^{+154}_{-117}
RCS 2319+0038	860 ± 190	1012^{+93}_{-97}

[a] Xue & Wu (2000).

redshift X-ray–selected clusters. The robustness and implications of this result are explored in detail in § 7.4.

Gas masses, total masses, and gas mass fractions can be found in Tables 7 and 8. We note that while extrapolations to larger radii are possible using our measured β fit parameters, R_{2500} is the radius to which we have confident measures for our entire sample.

7. CLUSTER SCALING RELATIONS

Studying the relationships between global cluster properties (L_X, T_X, M_{tot}, etc.) over a broad range in redshift allows us to investigate the influence of nongravitational processes on cluster formation and evolution. On a less grand scale, these relationships can also lead to interesting clues regarding an individual cluster's dynamical state and composition, as well as provide a method of comparison between different cluster samples. In this paper we investigate the evolution of scaling relationships over the redshift range $0.1 < z < 1.0$ and use them to characterize high-z optically selected RCS clusters ($0.6 < z < 1.0$).

To facilitate comparisons between the RCS clusters and lower redshift X-ray–selected samples, we make use of our previous *Chandra* analysis of the CNOC subsample of the EMSS (Hicks et al. 2006; Yee et al. 1996; Gioia et al. 1990). The CNOC sample was assembled primarily based on X-ray luminosity, with a cut at 2×10^{44} ergs s^{-1} in the original EMSS catalogs (Gioia et al. 1990), and covers a redshift range of $0.1 < z < 0.6$.

This sample is not well matched in redshift to our RCS clusters, but it is one of the best-studied moderate-redshift cluster samples today, with substantial information about both X-ray and optical properties available. Our previous analysis of this sample using the same methodology (Hicks et al. 2006) also allows us to make a confident comparison of our measurements.

All relationships (L_X-T_X, L_X-M_{tot}, M_{tot}-T_X, L_X-Y_X, and M_{tot}-Y_X) are fitted within either R_{2500} or R_{500}, have been scaled by the

cosmological factor $E_z = H(z)/H_0 = [\Omega_m(1 + z)^3 + \Omega_\Lambda]^{1/2}$, and are fitted with the form

$$\log_{10} Y = C1 + C2 \log_{10} X. \tag{9}$$

In all relationships T_X is in units of 5 keV, L_X is in units of 10^{44} ergs s^{-1}, total mass is in units of 10^{14} $M_\odot$, and Y_X ($\equiv M_g T_X$) is in units of 4×10^{13} $M_\odot$ keV. Best-fitting relationships are determined using the bisector modification of the BCES algorithm in Akritas & Bershady (1996), and we calculate scatter along the Y-axis as $[\Sigma_{i=1,N}(\log_{10} Y_i - C_1 - C_2 \log_{10} X_i)^2/N]^{1/2}$, facilitating comparisons to previous work (e.g., Ettori et al. 2004a).

In all fits the cluster RCS 0439−2904 was left out, due to spectroscopic indications (Gilbank et al. 2007; Cain et al. 2008) that it does not consist of a single virialized mass, but two closely spaced objects in projection along the line of sight. We perform fits at $\Delta = 2500$ on the individual samples, RCS ($0.62 < z < 0.91$) and CNOC ($0.17 < z < 0.55$), as well as combined data from all 23 clusters ($0.17 < z < 0.91$). At $\Delta = 500$ only the RCS data are fitted. All fits are then reproduced with the slope fixed at the expected self-similar value. The following discussions pertain to fits with two free parameters unless otherwise noted. Results from the fitting performed in this section can be found in Table 9, while Table 10 provides comparison fits from the literature.

7.1. *The L_X-T_X Relationship*

In the absence of significant preheating and/or cooling, theory predicts that cluster luminosities should scale as $L_{bol} \propto T^2$. However, observational studies have resulted in relationships that fall closer to $L_{bol} \propto T^3$ (White et al. 1997; Allen & Fabian 1998; Markevitch 1998; Arnaud & Evrard 1999). These departures from theoretically expected self-similar scaling laws indicate the effects of nongravitational processes, such as galaxy formation (Voit 2005). There is also interest in whether the L_X-T_X relationship evolves with redshift (Ettori et al. 2004a), which we investigate in this section along with the properties of our sample.

The best-fitting relationships and their scatter are given in Table 9 and are plotted in Figure 3. At both radii (R_{2500} and R_{500}), the slope of the RCS fit is found to be consistent with a predicted self-similar slope of 2. The CNOC sample, with a slope of 2.31 ± 0.31, is only marginally consistent with predicted scaling, but it does agree with other low-redshift L_X-T_X relationships. The main difference between the RCS and CNOC fits, however, is their normalization, which is significantly lower in the case of the RCS fit, translating into $(2.3 \pm 0.3) \times 10^{44}$ ergs s^{-1} at 5 keV, compared to

TABLE 7
MASS ESTIMATES ($\Delta = 2500$)

Cluster	n_0 (10^{-2} cm^{-3})	M_{gas} (10^{13} $M_\odot$)	M_{2500} (10^{13} $M_\odot$)	f_{gas}
RCS 0224−0002...............................	$0.329^{+0.009}_{-0.010}$	$0.42^{+1.59}_{-0.05}$	$12.15^{+1.59}_{-1.62}$	$0.035^{+0.005}_{-0.005}$
RCS 0439−2904...............................	$0.545^{+0.016}_{-0.016}$	$0.07^{+0.01}_{-0.01}$	$0.86^{+0.10}_{-0.10}$	$0.078^{+0.011}_{-0.010}$
RCS 1107−0523...............................	$1.972^{+0.058}_{-0.061}$	$0.33^{+0.04}_{-0.04}$	$7.88^{+0.88}_{-0.88}$	$0.042^{+0.006}_{-0.005}$
RCS 1326+2903	$0.323^{+0.010}_{-0.010}$	$0.10^{+0.01}_{-0.01}$	$2.97^{+0.54}_{-0.56}$	$0.034^{+0.008}_{-0.006}$
RCS 1326+2903 ($z = 1.01$)...............	$0.432^{+0.013}_{-0.014}$	$0.06^{+0.01}_{-0.01}$	$1.28^{+0.24}_{-0.24}$	$0.048^{+0.011}_{-0.008}$
RCS 1419+5326	$2.427^{+0.047}_{-0.048}$	$0.75^{+0.06}_{-0.06}$	$11.39^{+0.64}_{-0.65}$	$0.065^{+0.005}_{-0.005}$
RCS 1620+2929	$0.675^{+0.038}_{-0.035}$	$0.29^{+0.06}_{-0.07}$	$7.60^{+1.51}_{-1.45}$	$0.039^{+0.010}_{-0.008}$
RCS 2318+0034	$0.713^{+0.011}_{-0.012}$	$0.97^{+0.06}_{-0.06}$	$24.28^{+2.82}_{-2.92}$	$0.040^{+0.005}_{-0.005}$
RCS 2319+0030	$0.698^{+0.019}_{-0.019}$	$0.66^{+0.07}_{-0.07}$	$12.55^{+1.34}_{-1.35}$	$0.052^{+0.007}_{-0.006}$
RCS 2319+0038	$1.205^{+0.033}_{-0.033}$	$0.87^{+0.10}_{-0.10}$	$16.54^{+1.59}_{-1.60}$	$0.052^{+0.006}_{-0.006}$
RCS 2320+0033	$0.699^{+0.019}_{-0.019}$	$0.59^{+0.07}_{-0.07}$	$13.57^{+2.06}_{-2.10}$	$0.044^{+0.008}_{-0.007}$

TABLE 8
Mass Estimates ($\Delta = 500$)

Cluster	R_{500} (kpc)	M_{gas} ($10^{14}\,M_\odot$)	M_{500} ($10^{14}\,M_\odot$)	f_{gas}
RCS 0224−0002	819^{+103}_{-69}	$0.153^{+0.020}_{-0.019}$	$4.975^{+0.680}_{-0.692}$	$0.031^{+0.006}_{-0.005}$
RCS 0439−2904	350^{+41}_{-28}	$0.047^{+0.006}_{-0.006}$	$0.364^{+0.041}_{-0.042}$	$0.129^{+0.020}_{-0.018}$
RCS 1107−0523	665^{+64}_{-48}	$0.113^{+0.013}_{-0.013}$	$1.782^{+0.198}_{-0.200}$	$0.063^{+0.009}_{-0.008}$
RCS 1326+2903	544^{+119}_{-61}	$0.032^{+0.004}_{-0.004}$	$1.083^{+0.198}_{-0.203}$	$0.030^{+0.007}_{-0.006}$
RCS 1326+2903 ($z = 1.01$)	440^{+112}_{-50}	$0.042^{+0.005}_{-0.005}$	$0.912^{+0.170}_{-0.174}$	$0.046^{+0.011}_{-0.009}$
RCS 1419+5326	802^{+37}_{-28}	$0.218^{+0.018}_{-0.019}$	$2.600^{+0.147}_{-0.148}$	$0.084^{+0.007}_{-0.006}$
RCS 1620+2929	627^{+115}_{-74}	$0.091^{+0.014}_{-0.013}$	$2.342^{+0.409}_{-0.420}$	$0.039^{+0.009}_{-0.008}$
RCS 2318+0034	979^{+103}_{-77}	$0.199^{+0.028}_{-0.026}$	$12.936^{+1.988}_{-2.060}$	$0.015^{+0.004}_{-0.003}$
RCS 2319+0030	749^{+118}_{-59}	$0.264^{+0.031}_{-0.031}$	$3.181^{+0.339}_{-0.343}$	$0.083^{+0.012}_{-0.011}$
RCS 2319+0038	809^{+62}_{-55}	$0.264^{+0.032}_{-0.032}$	$4.007^{+0.384}_{-0.388}$	$0.066^{+0.009}_{-0.008}$
RCS 2320+0033	760^{+112}_{-73}	$0.184^{+0.025}_{-0.024}$	$2.823^{+0.585}_{-0.602}$	$0.065^{+0.018}_{-0.014}$
RCS 0439−2904	569^{+63}_{-43}	$0.100^{+0.013}_{-0.013}$	$0.619^{+0.070}_{-0.071}$	$0.161^{+0.028}_{-0.024}$

$5.5^{+1.1}_{-0.9} \times 10^{44}$ ergs s^{-1} for CNOC. Fits to the combined sample have significantly higher scatter and a much larger slope (2.90 ± 0.35), inconsistent with self-similar evolution. This is an interesting result: taken with the individual fits, it suggests that redshift evolution in the normalization of L_X-T_X could be perceived as evolution in its slope if the fitted sample covered a broad enough range of redshifts.

This speculation naturally leads us to the important question of whether this trend toward lower luminosity is due to the different selection of the RCS clusters, or to a general evolutionary trend with redshift. In Table 10 we list our fit parameters along with others taken from the literature. Since a number of these studies use measurements at R_{500}, we compare our fits using estimates extrapolated to this radius. The results of Allen et al. (2001)

TABLE 9
Fitting Parameters

Fit	Sample	$\Delta = 2500$			$\Delta = 500$		
		C_1	C_2	$\sigma_{\log Y}$	C_1	C_2	$\sigma_{\log Y}$
$E_z^{-1}L_X$-T_X	RCS	0.36 ± 0.06	2.05 ± 0.34	0.17	0.59 ± 0.05	1.79 ± 0.42	0.15
	RCS	0.45 ± 0.03	2.0 (fixed)	0.20	0.65 ± 0.03	2.0 (fixed)	0.19
	CNOC	0.74 ± 0.08	2.31 ± 0.31	0.18	...	...	...
	CNOC	0.85 ± 0.01	2.0 (fixed)	0.19	...	...	...
	Total	0.56 ± 0.07	2.90 ± 0.35	0.28	...	...	...
	Total	0.81 ± 0.01	2.0 (fixed)	0.33	...	...	...
$E_z^{-1}L_X$-E_zM_{tot}	RCS	-0.03 ± 0.04	1.38 ± 0.12	0.16	-0.20 ± 0.16	1.03 ± 0.28	0.24
	RCS	0.06 ± 0.02	1.33 (fixed)	0.19	-0.28 ± 0.02	1.33 (fixed)	0.33
	CNOC	0.44 ± 0.12	1.26 ± 0.21	0.20	...	...	...
	CNOC	0.48 ± 0.01	1.33 (fixed)	0.23	...	...	...
	Total	0.07 ± 0.10	1.77 ± 0.15	0.29	...	...	...
	Total	0.40 ± 0.01	1.33 (fixed)	0.33	...	...	...
E_zM_{tot}-T_X	RCS	0.29 ± 0.03	1.48 ± 0.27	0.09	0.76 ± 0.08	1.72 ± 0.65	0.22
	RCS	0.28 ± 0.03	1.5 (fixed)	0.10	0.69 ± 0.03	1.5 (fixed)	0.23
	CNOC	0.24 ± 0.02	1.83 ± 0.13	0.07	...	...	...
	CNOC	0.27 ± 0.01	1.5 (fixed)	0.08	...	...	...
	Total	0.28 ± 0.02	1.63 ± 0.18	0.09	...	...	...
	Total	0.27 ± 0.01	1.5 (fixed)	0.08	...	...	...
$E_z^{-9/5}L_X$-Y_X	RCS	0.32 ± 0.05	0.73 ± 0.05	0.11	0.22 ± 0.04	0.65 ± 0.10	0.11
	RCS	0.40 ± 0.03	1.1 (fixed)	0.22	0.08 ± 0.03	1.1 (fixed)	0.27
	CNOC	0.50 ± 0.08	0.80 ± 0.09	0.12	...	...	...
	CNOC	0.29 ± 0.01	1.1 (fixed)	0.20	...	...	...
	Total	0.41 ± 0.03	0.88 ± 0.04	0.14	...	...	...
	Total	0.30 ± 0.01	1.1 (fixed)	0.22	...	...	...
$E_z^{2/5}M_{\mathrm{tot}}$-$Y_X$	RCS	0.25 ± 0.03	0.52 ± 0.05	0.06	0.43 ± 0.08	0.64 ± 0.22	0.23
	RCS	0.23 ± 0.03	0.581 (fixed)	0.09	0.37 ± 0.03	0.581 (fixed)	0.25
	CNOC	0.05 ± 0.04	0.63 ± 0.05	0.08	...	...	...
	CNOC	0.04 ± 0.02	0.581 (fixed)	0.09	...	...	...
	Total	0.18 ± 0.02	0.49 ± 0.03	0.10	...	...	...
	Total	0.04 ± 0.02	0.581 (fixed)	0.14	...	...	...

Notes.—Best fits to scaling relations cosmologically corrected by the factor E_z. Temperature is in units of 5 keV; luminosity in units of 10^{44} ergs s^{-1}; mass in units of $10^{14}\,M_\odot$; Y_X in units of $4 \times 10^{13}\,M_\odot$ keV. Scatter along the Y-axis is calculated as $[\Sigma_{i=1,N} (\log Y_i - C_1 - C_2 \log X_i)^2/N]^{1/2}$.

TABLE 10
FITTING COMPARISONS

Sample	C_1	C_2	Redshift
	$E_z^{-1}L_X$-T_X		
$\Delta = 2500$:			
RCS....................	0.36 ± 0.06	2.05 ± 0.34	$0.6 < z < 1.0$
CNOC	0.74 ± 0.08	2.31 ± 0.31	$0.1 < z < 0.6$
Total	0.56 ± 0.07	2.90 ± 0.35	$0.1 < z < 1.0$
ASF01	$0.98^{+0.09}_{-0.10}$	2.08 ± 0.06	$0.1 < z < 0.45$
$\Delta = 500$:			
RCS....................	0.59 ± 0.05	1.79 ± 0.42	$0.6 < z < 1.0$
ETB04	0.50 ± 0.11	3.72 ± 0.47	$0.4 < z < 1.3$
	$Ez^{-1}L_X$-E_zM_{tot}		
$\Delta = 500$:			
RCS....................	-0.20 ± 0.16	1.03 ± 0.28	$0.6 < z < 1.0$
ETB04	-0.63 ± 0.32	1.88 ± 0.42	$0.4 < z < 1.3$
	E_zM_{tot}-T_X		
$\Delta = 2500$:			
RCS....................	0.29 ± 0.03	1.48 ± 0.27	$0.6 < z < 1.0$
CNOC	0.24 ± 0.02	1.83 ± 0.13	$0.1 < z < 0.6$
Total	0.28 ± 0.02	1.63 ± 0.18	$0.1 < z < 1.0$
APP05	0.23 ± 0.05	1.70 ± 0.07	$z \leq 0.15$
ASF01	0.27 ± 0.34	1.51 ± 0.27	$0.1 < z < 0.45$
$\Delta = 500$:			
RCS....................	0.76 ± 0.08	1.72 ± 0.65	$0.6 < z < 1.0$
FRB01	0.52 ± 0.45	1.78 ± 0.10	$z < 0.09$
APP05	0.58 ± 0.14	1.71 ± 0.09	$z \leq 0.15$
KV05...................	0.51 ± 0.31	1.79 ± 0.19	$0.4 < z < 0.7$
ETB04	0.59 ± 0.05	1.98 ± 0.3	$0.4 < z < 1.3$
	$E_z^{-9/5}L_X$-Y_X		
$\Delta = 500$:			
RCS....................	0.22 ± 0.04	0.65 ± 0.10	$0.6 < z < 1.0$
M07....................	-0.10 ± 0.04	1.1 ± 0.04	$0.1 < z < 1.3$
	$E_z^{2/5}M_{tot}$-Y_X		
$\Delta = 500$:			
RCS....................	0.43 ± 0.08	0.64 ± 0.22	$0.6 < z < 1.0$
APP07	0.17 ± 0.2	0.55 ± 0.03	$z \leq 0.15$
KVN06...............	0.27 ± 0.006	0.581 ± 0.009	Theory

REFERENCES.—(APP05) Arnaud et al. 2005; (APP07) Arnaud et al. 2007; (ASF01) Allen et al. 2001; (BMS04) Borgani et al. 2004; (ETB04) Ettori et al. 2004a; (FRB01) Finoguenov et al. 2001; (KV05) Kotov & Vikhlinin 2005; (KVN06) Kravtsov et al. 2006; (M07) Maughan 2007; (SPF03) Sanderson et al. 2003.

from a selected sample of $0.1 < z < 0.5$ clusters are consistent in slope with our individual sample fits, but even higher in normalization than the CNOC fit. This is perhaps not surprising given that the clusters in their sample are relaxed lensing clusters, many of which have strong cooling cores that can significantly increase the central cluster luminosity. In general, we do not here have enough information to excise cooling cores from the RCS data; however, in the CNOC data, we did attempt to remove these features from the cluster temperatures and luminosities (Hicks et al. 2006). Discrepancies between CNOC and RCS are thus not likely to be due to a higher incidence of cooling cores in the lower redshift sample.

We also compare our sample to the $0.4 < z < 1.3$ X-ray–selected sample in Ettori et al. (2004a), which consists of 28 clusters taken from the *Chandra* archive. At $\Delta = 500$, they find that

the slope of the L_X-T_X relationship is much steeper than that predicted by self-similar scaling (slope $= 3.72 \pm 0.47$; Fig. 3), suggesting a negative redshift evolution in the relationship (i.e., clusters at high z have lower L_X for a given T_X). A similar result is suggested by Ettori et al. (2004b) based on simulations guided in part by low-redshift observations.

Figure 3 shows the extrapolation of our data to R_{500}. Seven of our nine objects lie on the Ettori et al. (2004a) relationship, suggesting at least some agreement between the properties of their X-ray–selected and our optically selected samples. We note that in general their higher redshift clusters also trend toward lower luminosities. While the slope of our fit to the RCS sample at $\Delta = 500$ is inconsistent with theirs, the slope of our combined $\Delta = 2500$ sample is in agreement with their slope, another indication that we may be resolving evolution in slope into changes in the normalization of the relationship with redshift. Our scatter for the individual fits is significantly lower than theirs ($\sigma_{\log Y} \leq 0.20$ vs. $\sigma_{\log Y} = 0.35$), whereas our scatter for the combined fits becomes more comparable (0.28). Thus, the RCS high-redshift sample appears to be at least qualitatively similar to this high-redshift X-ray–selected sample, in support of a trend for samples of clusters at high redshift to have lower luminosities at a given temperature.

In summary, the slope of the L_X-T_X relation from our high-redshift RCS sample is consistent with lower redshift X-ray–selected samples (Allen et al. 2001) and the predictions of self-similarity, while the slope of our combined $0.1 < z < 1.1$ sample is in agreement with the results of similarly broad ($0.4 < z < 1.3$) X-ray–selected samples (Ettori et al. 2004a).

7.2. The L_X-M_{tot} Relationship

On examining the cosmologically corrected L_X-M_{tot} relationship, we again see disparity between the normalizations of the CNOC and RCS fits. This finding provides additional evidence that there is less gas for a given total mass in our high-redshift sample. Individual slopes at R_{2500} agree with the self-similar value of 1.33, while the slope of the combined sample fit is higher and inconsistent with that value (Table 9; Fig. 4). Our RCS fit at R_{500} is again consistent in normalization, but not slope, with Ettori et al. (2004a). Likewise, again our combined (R_{2500}) sample slope (1.77 ± 0.15) agrees well with theirs (1.88 ± 0.42). Our scatter ($0.16 \leq \sigma_{\log Y} \leq 0.33$) is lower in all cases.

7.3. The M_{tot}-T_X Relationship

The M_{tot}-T_X relationship is by far the lowest scatter ($\sigma_{\log Y} \leq 0.10$) relationship in this work (Fig. 5), although this is largely because of the degeneracy between the two parameters, with much of the scatter arising from differences in the spatial distribution of gas. All of our fits at R_{2500} have consistent normalizations, and all but the CNOC fit have slopes that agree well with self-similar predictions. Although the CNOC slope is higher (1.83 ± 0.13), it is in good agreement with both of our listed R_{2500} comparison fits (Allen et al. 2001; Arnaud et al. 2005), as are the fits of both the RCS sample and the combined sample (Table 10).

At R_{500} the RCS fit is in agreement with Finoguenov et al. (2001), Arnaud et al. (2005), and Kotov & Vikhlinin (2005). Our normalization is somewhat higher, however, than all of theirs, and it is in disagreement with that of Ettori et al. (2004a) (Fig. 5). The three objects that are most responsible for driving up the normalization all have gas distributions that appear to be more concentrated than average ($\beta \geq 0.72$; Table 3), which would tend to drive up the total mass at higher radius, noting again that at R_{500} our masses are extrapolations. In addition, the two most outlying
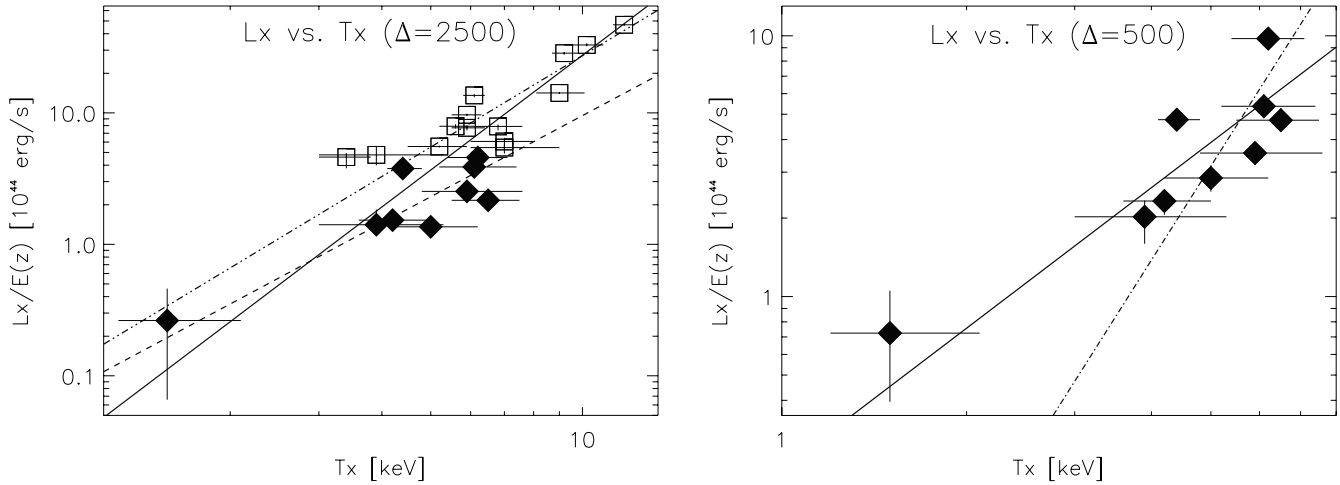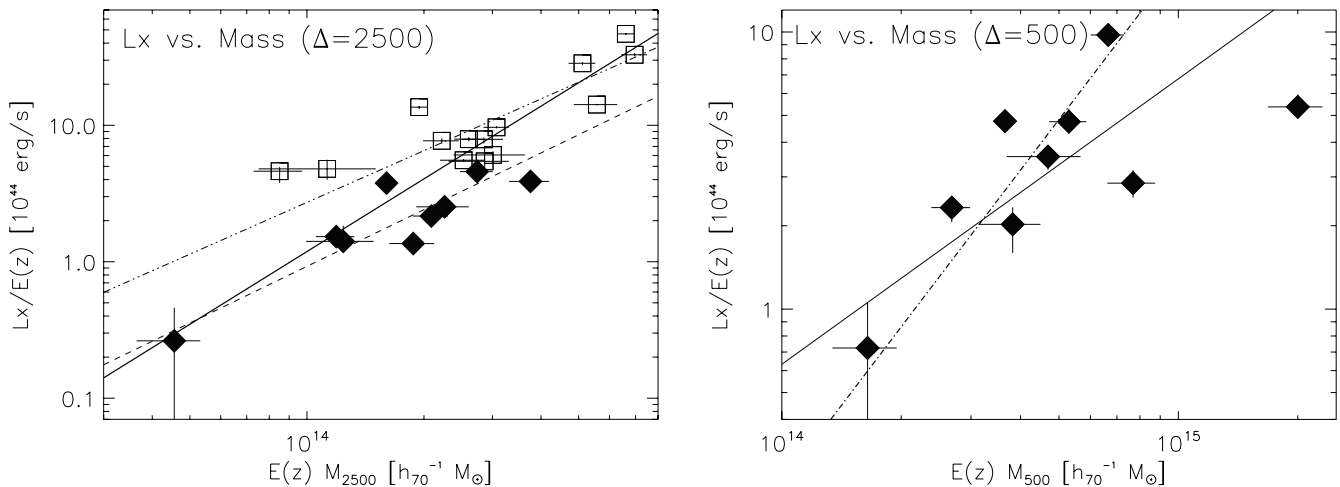
FIG. 3.—*Left*: X-ray temperatures plotted against cosmologically corrected unabsorbed bolometric luminosities within R_{2500}. Squares designate moderate-redshift CNOC clusters ($z_{avg} = 0.32$), and diamonds represent high-z RCS clusters ($z_{avg} = 0.80$). The dashed line traces the best-fitting relationship for only the RCS clusters, which has a slope of 2.05 ± 0.3, and the double-dot–dashed line denotes the best fit to the CNOC data with a power-law slope of 2.3 ± 0.3, both in agreement with self-similar expectations. The solid line indicates the best-fitting relationship for the entire sample, with a slope of 2.9 ± 0.3, inconsistent with the self-similar value, but in marginal agreement with Ettori et al. (2004a), who find 3.7 ± 0.5 for a cluster ensemble with $0.4 < z < 1.3$. *Right*: L_X vs. T_X at $\Delta = 500$. The solid line denotes our best-fitting relationship for the RCS clusters with slope 1.8 ± 0.4, again consistent with self-similar scaling. The dot-dashed line shows the fit of Ettori et al. (2004a), which was also measured within R_{500}. Seven of our nine objects lie on their relationship, suggesting at least some agreement between the properties of their X-ray–selected and our optically selected samples. [*See the electronic edition of the Journal for a color version of this figure.*]

points consist of our least massive cluster (RCS 1326+2903, also our weakest detection in the detailed analysis sample) and our most massive cluster (RCS 2318+0034). It is worth mentioning again that in Figure 1, the brightest part of RCS 2318+0034 does not seem to lie at the center of the cluster's extended emission, indicating that this object may have recently undergone a merger, or could at least possess an appreciable amount of substructure.

7.4. *Gas Mass Fractions*

In § 6 we estimate the core (R_{2500}) gas mass fractions of our high-z sample, finding values that are significantly lower than both the core gas fractions of lower redshift X-ray–selected clusters and the expected universal gas fraction ($\Omega_b/\Omega_m = 0.175 \pm 0.012$; Spergel et al. 2007). Taking a weighted average over our high-z objects results in a core gas mass fraction of $4.5\% \pm 0.2\%$,

in comparison with the CNOC weighted mean of $9.8\% \pm 0.3\%$ and values of $\sim9\%$ found within R_{2500} in clusters with $T_X > 5$ keV (Vikhlinin et al. 2006). To estimate the contribution of possible mass overestimation on the magnitude of these discrepancies, we also calculate a weighted average using only objects for which $\beta \leq 0.65$, resulting in a fraction of $5.1\% \pm 0.3\%$, which remains significantly low. Poor clusters and groups are often found to have lower gas mass fractions (Dell'Antonio et al. 1995; Sanderson et al. 2003); therefore, we may expect this result for the lower temperature objects in our sample. This, however, does not explain our findings for the higher temperature objects.

To investigate further, we first performed a K-S test on the f_g values of subsets of both samples, choosing the eight objects in the RCS sample and the nine objects in the CNOC sample with temperatures between 3.5 and 8 keV. This test resulted in

FIG. 4.—*Left*: X-ray mass plotted against cosmologically corrected unabsorbed bolometric luminosity within R_{2500}. Diamonds designate high-redshift RCS clusters, and squares represent moderate-redshift CNOC clusters. The dashed line traces the best-fitting relationship for only the RCS clusters, which has a slope of 1.4 ± 0.1, while the double-dot–dashed line denotes the best fit to the CNOC data with a power-law slope of 1.3 ± 0.2, both again in excellent agreement with the self-similar slope of 1.33. The solid line indicates the best-fitting relationship for the combined sample, which again has a higher slope of 1.77 ± 0.15. *Right*: Our L_X-M_{500} data plotted with both our relationship (*solid line*; slope 1.03 ± 0.28) and that of Ettori et al. (2004a) (*dot-dashed line*; slope 1.88 ± 0.42) overlaid. [*See the electronic edition of the Journal for a color version of this figure.*]
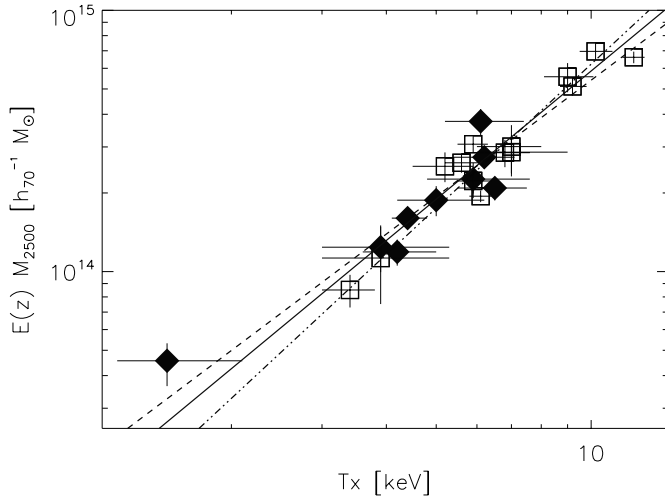
FIG. 5.—X-ray temperatures plotted against cosmologically corrected mass estimates from § 6. Squares designate the CNOC clusters ($0.1 < z < 0.6$), and diamonds represent RCS clusters ($0.6 < z < 1.0$). The dashed line indicated the RCS fit, with a slope of 1.5 ± 0.3. Fits to the entire sample (*solid line*) are also consistent with self-similar evolution (slope 1.6 ± 0.2). The CNOC fit has a higher slope (*double-dot–dashed line*; 1.83 ± 0.13) but is in good agreement with those from the literature (Allen et al. 2001; Arnaud et al. 2005). [*See the electronic edition of the Journal for a color version of this figure.*]

$D = 0.875$ and $P = 0.002$, indicating that the gas mass fractions of the two samples are different at a confidence level of greater than 99%. A histogram showing the f_g distributions of these subsamples is shown in Figure 6.

We examined the robustness of this result by repeating the K-S test after attempting to remove the effects of any possible trend in gas fraction with temperature. To do so, we assumed that the RCS and CNOC samples can be combined and that the resulting apparent trend of f_{gas} with temperature is physical (note that the resulting relation is much steeper than the one suggested by Vikhlinin et al. 2006; Fig. 6). Under these extreme assumptions, the K-S test yields $D = 0.764$ and $P = 0.007$, thus demonstrating the robustness of our earlier results.

Low gas mass fractions have previously been observed in clusters at high redshift by both the *XMM-Newton* Ω project (Sadat

et al. 2005) and Lubin et al. (2002) and have been predicted in simulations of high-redshift objects (Nagai et al. 2007; Ettori et al. 2004b, 2006; Kravtsov et al. 2005). In addition, an SZ/*WMAP* study performed by Afshordi et al. (2007) reports that ~35% of expected baryonic mass is missing from the hot intracluster medium (ICM) in their 193 clusters. Redshift evolution, however, may not be the only possibility. Multiple studies have confirmed that at least some fraction of their optically selected clusters have lower than expected L_X (e.g., Bower et al. 1994; Donahue et al. 2002; Gilbank et al. 2004; Popesso et al. 2007); therefore, sample selection may also contribute to this effect. We explore selection biases in more depth in § 9.

Given the possibilities present in the literature and a current lack of sufficient data to perform direct comparisons with significant samples matched in both mass and redshift, it is difficult to determine conclusively that the low gas fractions measured here are the result of cluster evolution. Possible physical explanations for lower gas fractions are that our clusters have a comparatively higher amount of baryonic matter in the form of stars (Vikhlinin et al. 2006; Nagai et al. 2007), that gas is still infalling (i.e., in the process of virialization; Popesso et al. 2007), or that some mechanism has injected excess energy into the gas (i.e., galaxy formation, mergers, active galactic nuclei [AGNs], radio jets; Nulsen et al. 2005), thereby raising its entropy at high z. Many of these processes occur with relatively higher frequency at high redshift (e.g., Lacey & Cole 1993; Eastman et al. 2007); thus, a general trend toward lower gas fractions might easily be expected in high-z clusters.

7.5. *Cluster Entropy*

Cluster entropy can be used as a tool for investigating the energy budget of baryons in clusters (Ponman et al. 1999). Because it may provide insight into f_{gas} discrepancies, we investigate it here for our two samples. Thermodynamic entropy is proportional to the log of the measurable quantity $S \equiv T_X/n_e^{2/3}$. The canonical radius for measuring S is $0.1R_{200}$ (Ponman et al. 1999), so that is the radius at which we present it here.

Figure 7 shows a plot of cosmologically corrected entropy ($E_z^{4/3}S$) versus temperature, with the relationship of Ponman et al. (2003) overlaid ($S \simeq 120T_X^{0.65}$ keV cm^2). The specific entropy of the RCS clusters seems overall to be slightly higher for a given
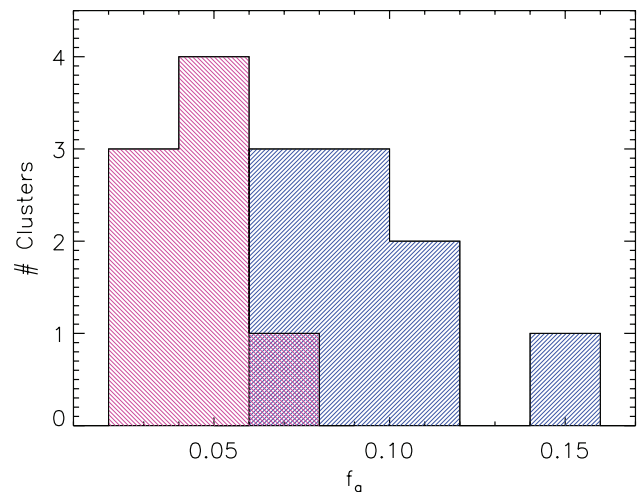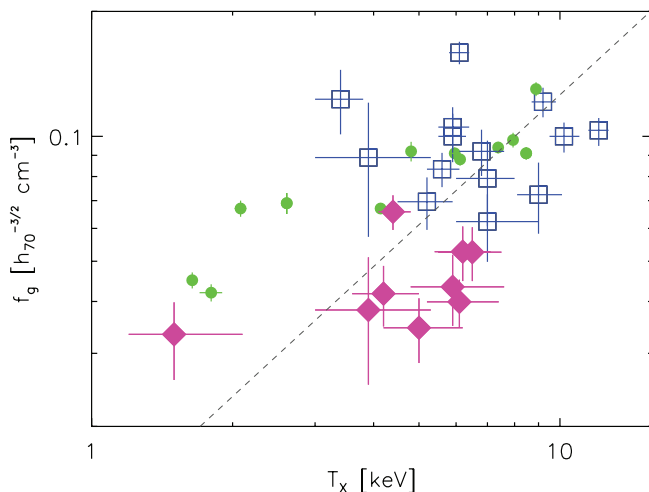

FIG. 6.—*Left*: T_X plotted against gas mass fractions within R_{2500}. Squares designate moderate-redshift CNOC clusters ($0.1 < z < 0.6$), and diamonds represent higher z RCS clusters ($0.6 < z < 1.0$). The dashed line indicates the best-fitting relationship for the entire sample, with a slope of 1.0 ± 0.2. Circles indicate points taken from Vikhlinin et al. (2006). *Right*: Histogram of gas mass fractions for the eight RCS (*left side*) and nine CNOC clusters (*right side*) with 3.5 keV $< T_X < 8$ keV. A K-S test performed on these two samples resulted in $D = 0.875$ and $P = 0.002$, indicating that the gas mass fractions of the samples are different at >99% confidence.
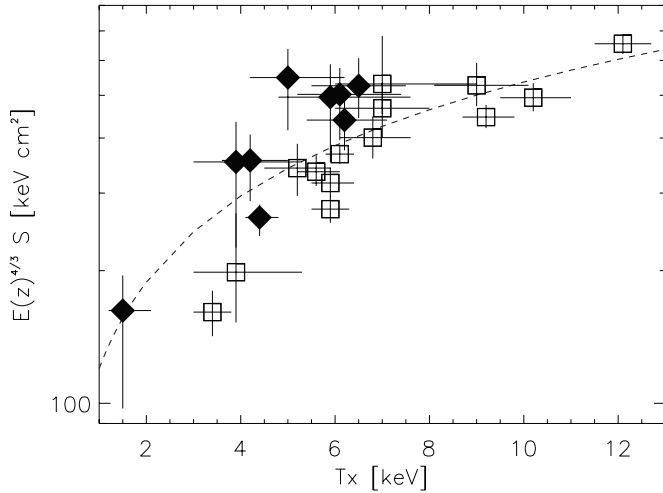
Fig. 7.—Entropy measured at $0.1R_{200}$ plotted against X-ray temperature for the clusters in this study. RCS clusters (*diamonds*) have slightly higher entropies for a given T_X than CNOC clusters (*squares*), although probably not enough to account for the whole of the discrepancies seen in gas fractions between the samples. The dashed line indicates the relationship of Ponman et al. (2003). [*See the electronic edition of the Journal for a color version of this figure.*]

Fig. 8.—Y_X plotted against X-ray luminosity within R_{2500}. Although CNOC (*squares and double-dot–dashed line*) and RCS (*diamonds and dashed line*) slopes agree, their normalizations are inconsistent, probably due to differences in gas mass fractions between the two samples. The solid line indicates the best-fitting relationship for the entire sample. Overall this is the tightest relationship involving L_X that we investigate in this work. [*See the electronic edition of the Journal for a color version of this figure.*]

temperature than that of the CNOC sample. A K-S test on the clusters with 3.5 keV $< T_X < 8.0$ keV results in $D = 0.431$ and $P = 0.208$, indicating a difference between the samples at a $\sim 80\%$ confidence level.

As in the case of the gas mass fractions, we perform an additional K-S test after attempting to remove the trend in cluster entropy with temperature. Using the relationship of Ponman et al. (2003) (above), the K-S test yields $D = 0.764$ and $P = 0.007$, indicating a systematic difference in the entropies of the two samples at a $>99\%$ level. Weighted means of the corrected (5 keV) entropies of the two K-S sample subsets result in $S_{CNOC} = 297 \pm 9$ keV cm^2 and $S_{RCS} = 425 \pm 18$ keV cm^2, with the RCS clusters having higher entropy on average by a factor of 1.43. Because f_g is proportional to gas density, at a constant temperature $f_g \propto S^{3/2}$; therefore, differences in entropy between the two samples can account for roughly 85% of their f_g discrepancy, indicating that additional factors may be in effect as well.

It remains difficult to determine the relative contributions of evolution and selection to possible differences in entropy. Expectations of higher merger and AGN activity at high z (Lacey & Cole 1993; Eastman et al. 2007) suggest that an evolutionary explanation is feasible; however, X-ray surveys that select high central density objects may be prone to preferentially pick out low-entropy systems.

7.6. Y_X Relationships

The product of cluster temperature and gas mass, $Y_X = M_g T_X$, has been shown in simulations to be a reliable, low-scatter proxy for total cluster mass and to be well correlated to X-ray luminosity (Kravtsov et al. 2006; Maughan 2007). Here we investigate relationships between these quantities and Y_X for our high-redshift optically selected sample. We adopt self-similar E_z scaling from Maughan (2007) and Kravtsov et al. (2006) for the L_X and mass relationships, respectively, and use their best-fitting slopes for our constrained slope fits.

Our individual samples can be seen to lie again on two separate relationships in the Y_X-L_X plane, of similar slope and differing normalization (Fig. 8). This can once more be explained as stemming from systematically lower gas mass fractions in the RCS sample. We cannot make normalization comparisons to Maughan
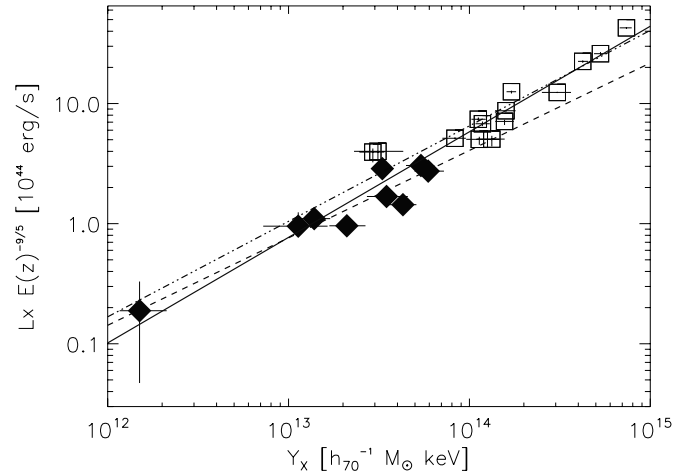
(2007) at R_{2500}; however, none of the slopes of our L_X-Y_X fits are consistent with the slope resulting from fits to his overall sample, and when we fix the slope to his value, our scatter increases by a factor of ~ 2. At R_{500} our fit to the RCS data agrees neither in slope nor in normalization with his fit (Fig. 8), but again it should be mentioned that our R_{500} values have been extrapolated from data within R_{2500}.

There is an even more significant discrepancy between the normalizations of the CNOC and RCS samples in the Y_X-M_{tot} relationship. This is easily explained as we are already aware that gas mass fractions are lower in the RCS sample, and total mass versus Y_X ($\propto M_{gas}$) highlights this difference. We find overall closer agreement with the slope of the Y_X-M_{tot} relationship modeled by Kravtsov et al. (2006) than we did in the case of L_X-Y_X. Here we see marginal agreement at R_{2500} between their R_{500} slope and that of the RCS fit, as well as consistency with the slope of the CNOC sample relationship. At R_{500}, although the slope of the RCS fit is still consistent with theirs, the normalizations disagree. The reason for this is illustrated nicely in the right panel of Figure 9. The four clusters in our sample that do not lie on their relationship are those with the lowest gas mass fractions. And again we see that the three biggest outliers are those with the highest β-values, and that of these, the two most discrepant are RCS 1326+2903 and RCS 2318+0034.

8. CORRELATIONS WITH OPTICAL RICHNESS

Optical richness is effectively a measurement of galaxy overdensity within a given aperture, normalized for the evolving galaxy luminosity function and the expected spatial distribution of galaxies in the cluster. Our chosen richness measurement, B_{gc} (Yee & Lopez-Cruz 1999), represents the galaxy-cluster spatial covariance amplitude (Longair & Seldner 1979),

$$\xi(r) = \left(\frac{r}{r_0}\right)^{-\gamma} = B_{gc} r^{-\gamma}. \tag{10}$$

In practice, B_{gc} is based on the excess number counts of galaxies within 357 kpc of the cluster optical center, with a normalization applied to correct for the expected spatial distribution (here we assume $\gamma = 1.8$, which is in general agreement with
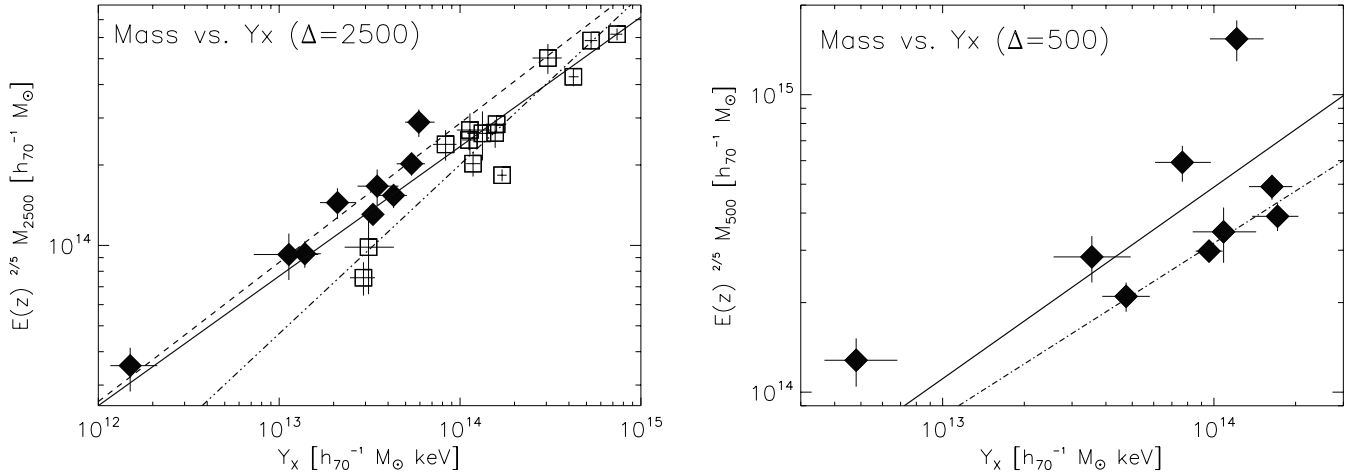
Fig. 9.—*Left*: Y_X plotted against mass estimates within R_{2500}. Here we find marginal agreement between the slopes of our individual fits, CNOC (*squares and double-dot–dashed line*) and RCS (*diamonds and dashed line*), and the slope of Kravtsov et al. (2006). *Right*: Y_X-M_{tot} relationship fitted for RCS clusters at $\Delta = 500$ (*solid line*). In a direct comparison with Kravtsov et al. (2006) (*dot-dashed line*), our slopes are in agreement but normalizations are inconsistent. The points that do not lie on their relationship are also the clusters that have the lowest gas mass fractions in our sample. Bear in mind that we are extrapolating to get out to R_{500}, as our data mostly lie within R_{2500}. [*See the electronic edition of the Journal for a color version of this figure.*]

actual galaxy distributions at these radii) and for the evolving luminosity function of cluster galaxies. Although some uncertainties exist in the evolution of cluster galaxies at redshifts of $z > 0.5$, they can be minimized by employing a red-sequence optical richness, $B_{gc,red}$, which is calculated using only the more uniformly evolving red galaxies in a cluster, and which may be better correlated with the underlying cluster mass. This is the optical richness parameter that is used throughout this work. Values of $B_{gc,red}$ for this sample are given in Table 5.

It has been shown that B_{gc} correlates well with the X-ray parameters of relaxed clusters (Yee & Ellingson 2003), and in Hicks et al. (2006) we have derived relationships for correlations of X-ray properties with $B_{gc,red}$. These relationships, however, were calibrated for X-ray–selected clusters at moderate redshift and therefore may not accurately describe our current sample. Here we test these correlations for optically selected clusters at high redshift. In the following we assume that $B_{gc,red}$ behaves similarly to the X-ray temperature when comparing to the X-ray properties. The rationale for this choice is that for a cluster with a fixed density profile, both the temperature and $B_{gc,red}$ do not change with redshift, whereas M_{2500}, L_X, etc., do change (following self-similar evolution).

Our actual data do not extend much beyond R_{2500}, so most of our fitting is performed within that radius. Cluster properties included in our fits are L_X, T_X, and total mass. Again we employ the BCES algorithm of Akritas & Bershady (1996). For each of our fits we adopt the form

$$\log_{10} Y = C_1 + C_2 \log_{10} B_{gc,red}, \qquad (11)$$

where Y represents the particular property being fitted. For L_X, T_X, and total mass, units of 10^{44} ergs s^{-1}, 5 keV, and 10^{14} $M_\odot$ were used, respectively. RCS 0439−2904 was again removed from fitting procedures, as it has been confirmed to be two closely spaced systems in projection along the line of sight (Gilbank et al. 2007; Cain et al. 2008). Best-fitting parameters and scatters are given in Table 11, along with comparison fits from the literature.

Figure 10 shows the relationship between temperature and richness. Here there is little evidence for a systematic difference between the samples, with both the CNOC and the combined sample showing statistical agreement with the expected slope of $2/\gamma =$

1.11 (Yee & Ellingson 2003). The RCS sample is on average slightly cooler at a given $B_{gc,red}$, a tendency that might stem from sample selection (see § 9). Note that both X-ray–selected and optically selected samples contain a few outliers, scattering toward higher temperature or lower richness. Figure 11 shows relationships

TABLE 11
$B_{gc,red}$ Fitting Parameters

Fit	Sample	C_1	C_2	$\sigma_{\log Y}$
L_X	RCS	-10.40 ± 2.61	3.68 ± 0.89	0.39
	RCS	-6.10 ± 0.04	2.22 (fixed)	0.24
	CNOC	-5.88 ± 1.66	2.31 ± 0.55	0.32
	CNOC	-5.65 ± 0.02	2.22 (fixed)	0.32
	Total	-10.10 ± 2.29	3.68 ± 0.76	0.49
	Total	-5.65 ± 0.02	2.22 (fixed)	0.40
	YE03	-4.48 ± 0.75	1.84 ± 0.24	...
T_X	RCS	-5.54 ± 1.56	1.86 ± 0.54	0.21
	RCS	-3.35 ± 0.04	1.11 (fixed)	0.14
	CNOC	-2.90 ± 0.75	1.00 ± 0.24	0.14
	CNOC	-3.26 ± 0.02	1.11 (fixed)	0.16
	Total	-4.08 ± 0.94	1.38 ± 0.31	0.18
	Total	-3.28 ± 0.02	1.11 (fixed)	0.16
	YE03	-2.29 ± 0.4	0.78 ± 0.13	...
M_{2500}	RCS	-8.20 ± 3.11	2.86 ± 1.06	0.36
	RCS	-4.93 ± 0.04	1.67 (fixed)	0.22
	CNOC	-4.81 ± 1.51	1.75 ± 0.49	0.26
	CNOC	-4.66 ± 0.02	1.67 (fixed)	0.27
	Total	-6.31 ± 1.36	2.24 ± 0.45	0.30
	Total	-4.74 ± 0.02	1.67 (fixed)	0.28
M_{200}	RCS	-9.53 ± 6.20	3.54 ± 2.11	0.51
	RCS	-4.27 ± 0.04	1.67 (fixed)	0.30
	CNOC	-4.61 ± 1.53	1.88 ± 0.50	0.26
	CNOC	-4.06 ± 0.02	1.67 (fixed)	0.26
	Total	-5.86 ± 1.43	2.30 ± 0.48	0.32
	Total	-4.12 ± 0.02	1.67 (fixed)	0.28
	YE03	-4.55 ± 0.89	1.64 ± 0.28	...
	B07	-5.70 ± 3.4	2.1 ± 1.2	...

Notes.—Fits to richness scaling relationships. Luminosity is given in units of 10^{44} ergs s^{-1}, temperature in units of 5 keV, and mass in units of 10^{14} $M_\odot$. Parameters for the present work are measured within $\Delta = 2500$ unless otherwise noted. Scatter ($\sigma_{\log Y}$) is given as $[\Sigma_{i=1,N}(\log Y_i - C_1 - C_2 \log X_i)^2/N]^{1/2}$.
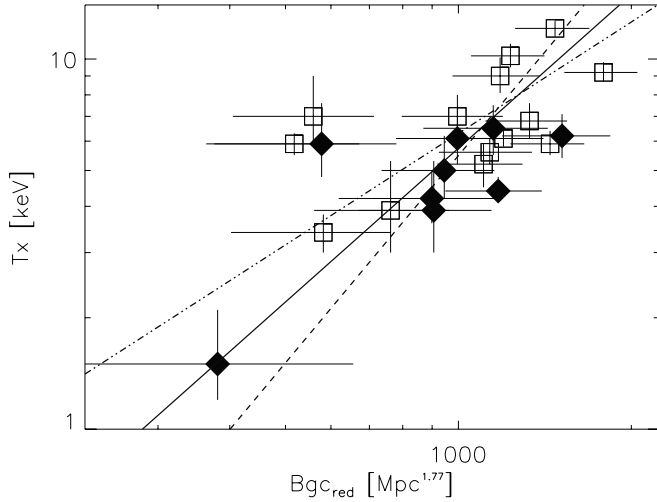References.—(B07) Blindert et al. 2007; (YE03) Yee & Ellingson 2003.

Fig. 10.—Log-log plot of T_X vs. $B_{gc,red}$ within R_{2500} for the CNOC (*squares*) and RCS (*diamonds*) samples. Error bars represent 68% confidence intervals. The fit to the combined sample (*solid line*) is in agreement with both the CNOC (*double-dot–dashed line*) and RCS (*dashed line*) fits. Both the CNOC and combined fits are also consistent in slope with the expected value of 1.11 (Yee & Ellingson 2003). These relationships, on average, show the lowest scatter of any richness relationships investigated in this work, with a lower average scatter even than L_X-T_X. The scatter of the RCS fit is mostly driven by the outlying point (RCS 2320+0033), which has a very low $B_{gc,red}$ for its mass. [*See the electronic edition of the Journal for a color version of this figure.*]

between richness, M_{2500} and M_{200}. At R_{2500} only the CNOC sample shows agreement with the expected slope of $3/\gamma$. All R_{200} fits are consistent with the values obtained for the CNOC sample by Yee & Ellingson (2003) using galaxy dynamics and the fit reported in Blindert et al. (2007) for a sample of 33 RCS clusters ($0.2 < z < 0.5$). The consistency between these fits indicates a general agreement between both the samples and the different mass estimators; however, it should also be noted that error bars on the fit parameters are quite large for this relationship.

The L_X-$B_{gc,red}$ plot (Fig. 12), in contrast, shows quite a bit of scatter for both samples and a significant offset between the RCS and CNOC samples. This offset is expected for the RCS sample, based on the results of § 7.1, but here we also include the addi-

tional clusters with low X-ray luminosity for which T_X could not be derived. RCS 0439−2904, the object that is spectroscopically confirmed to be a projection of two less massive systems, is the cross second from the right. The significantly higher amount of scatter that we see in this relationship when compared to any of the other L_X relationships suggests that $B_{gc,red}$ is a less reliable predictor of X-ray luminosity than T_X, total mass, or Y_X.

Of all the richness relationships we investigate, $B_{gc,red}$ is best correlated to X-ray temperature, with an average scatter (all fits) of only $\sigma_{\log Y} \sim 0.16$ for the objects with measured T_X (minus RCS 0439−2904, which is not included in fitting). When fitting mass to richness, overall scatters average (all fits) to $\sigma_{\log Y} = 0.28$ for M_{2500} and 0.32 for M_{200}. The scatter in the RCS sample at R_{200} is particularly large, due in part to the two objects with high β-values (RCS 1326+2903 and RCS 2318+0034) and RCS 2320+0033, which has a lower than expected $B_{gc,red}$. In its role as a mass estimator, $B_{gc,red}$ produces on average 0.07–0.19 more scatter in $\sigma_{\log Y}$ than the T_X-based mass proxies investigated here and may suffer from a fraction of objects whose richnesses are affected by projection. However, the comparative speed and ease with which it can be obtained still recommend it as a potentially useful tool for mass estimations of large high-redshift cluster samples.

9. SAMPLE SELECTION AND BIASES

The RCS sample is effectively selected by richness ($B_{gc,red}$), whereas the CNOC sample was compiled from objects with high X-ray luminosity (Yee et al. 1996). Discrepancies in the relations between X-ray and optical properties for these two samples may thus partially be caused by sample selection, especially if the underlying distribution of X-ray to optical properties is intrinsically broad (e.g., Gilbank et al. 2004). Both X-ray and optical surveys would then be expected to deliver biased samples of clusters, with the degree of bias based on the level of scatter in the selection criterion. Here we discuss three sources of selection bias in optical and X-ray cluster samples: optical projection effects, Eddington bias due to observational uncertainty, and sample bias for both optical and X-ray samples.

One important difference in the cluster samples stems from the RCS cluster-finding process. While all but one of our objects
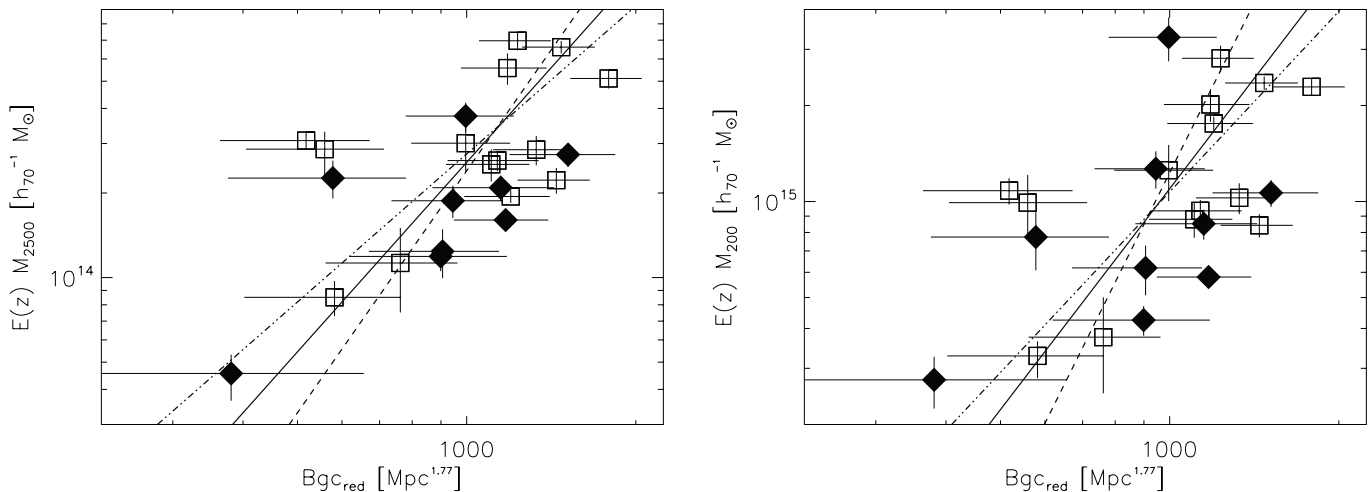

Fig. 11.—*Left*: Total mass plotted against $B_{gc,red}$ for $R < R_{2500}$. Error bars represent 68% confidence intervals. CNOC clusters are shown as squares, and diamonds designate the RCS sample. The dashed line shows the best relationship for the RCS sample, while double-dot–dashed and solid lines indicate fits to the CNOC and combined samples, respectively. The average scatter in the relationships is $\sigma_{\log Y} = 28\%$; however, all fits are consistent with one another due to large errors. *Right*: $B_{gc,red}$ vs. M_{200}. X-ray masses were extrapolated to R_{200} for comparison with the relationship of Blindert et al. (2007). All three of our fits are consistent with their relationship, which was determined via dynamical investigations of 33 moderate-redshift RCS clusters. Scatter in our fits averages to 32%. [*See the electronic edition of the Journal for a color version of this figure.*]
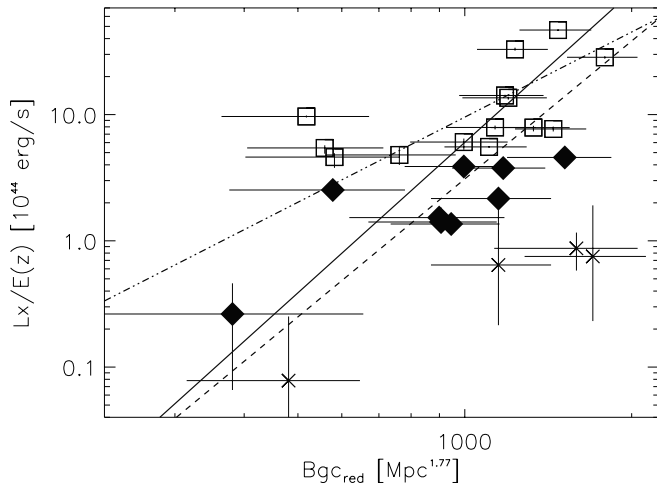
Fig. 12.—Log-log plot of L_X vs. $B_{gc,red}$ for the combined CNOC/RCS sample. CNOC clusters are shown as squares, and diamonds designate RCS clusters that are included in fitting. Crosses indicate the four clusters that were not included in fitting due to nondetection (*cross farthest to the left*), known superposition (RCS 0439−2904; *cross second from the right*), or insufficient counts (*remaining two crosses*). Luminosities for these objects (excluding RCS 0439−2904) were determined in XSPEC assuming a temperature of 4 ± 2 keV. Error bars represent 68% confidence intervals. A dashed line shows the RCS sample fit, while double-dot–dashed and solid lines indicate CNOC and combined sample fits, respectively. On average, these relationships show the most scatter of all those that we investigate in this work. [*See the electronic edition of the Journal for a color version of this figure.*]

were confirmed (to S/N > 3) as extended X-ray sources, the RCS sample is expected to also include a small fraction of objects whose richness is boosted by the superposition of other structures having galaxy colors similar to the cluster's red sequence. While these projections are much less problematic than in monochromatic cluster searches, they may still add systems into the RCS catalog with true richnesses significantly lower than the measured $B_{gc,red}$. Gladders (2002) performed a series of simulations that suggest that the fraction of RCS clusters composed of significant projections is on the order of 5%–10%. This estimate has been confirmed at $z \sim 0.3$ via extensive spectroscopy of 33 RCS clusters (Blindert et al. 2007) and at $z \sim 0.8$ from a sample of 12 clusters (Gilbank et al. 2007). Additional spectroscopy, as well as weak-lensing estimates of additional clusters, is underway. Recently, Cohn et al. (2007) examined the effects of local structures on the red sequence using the Millennium cosmological simulations. They found that in the simulation, the frequency of significant projection increases at higher redshift, to $\sim$20% at $z = 1$. However, their cluster-finding algorithm and richness estimate were significantly different from the RCS algorithm in many aspects (galaxy magnitudes and colors, radial extent, and background corrections), so this may not be directly comparable to the samples discussed here.

Our *Chandra* observations suggest that perhaps 3 of 13 observed clusters may have X-ray luminosities that are significantly lower than expected from the RCS L_X-$B_{gc,red}$ relationship. All three of the outliers in Figure 12 have been observed in detail spectroscopically, and two of these were found to have at least some degree of overlap with additional structures in the line of sight. RCS 0439−2904 was found spectroscopically to consist of two objects in such close proximity that they may be interacting (Gilbank et al. 2007; Cain et al. 2008). RCS 1417+5305 is a similar case, although here the overlapping systems are different enough in redshift that they might be unrelated (Gilbank et al. 2007). RCS 2112−6326 exhibits a single spectroscopic peak at

$z \sim 1.1$ (L. F. Barrientos et al. 2008, in preparation). It is not clear whether the highest richness systems in this sample might be subject to a higher contamination rate than the RCS-1 survey as a whole.

Because there is significant observational uncertainty in our richness estimates, and the number of clusters declines rapidly with increasing richness, it is also necessary to evaluate effects of a possible Eddington bias in the X-ray/optical relationships. We calculate this possible bias by using the observed distribution of $B_{gc,red}$ in the RCS-1 sample, which falls as $B_{gc,red}^N$, where $N \sim -4$. Uncertainties in $B_{gc,red}$ are calculated based on the statistics of galaxy counts in the clusters and in the statistical foreground/background galaxy distribution (Yee & Lopez-Cruz 1999) and tend to increase modestly with increasing richness. We model the typical Gaussian 1σ uncertainty in $B_{gc,red}$ as a function of $B_{gc,red}$ from an empirical fit to the observed distribution in RCS-1:

$$\log_{10}(\sigma) = 0.899 + 0.535 \log_{10}\left(B_{gc,red}\right). \quad (12)$$

This relationship predicts that the uncertainty will be $\sim$180 at $B_{gc,red} = 300\ h_{50}^{-1}\ \mathrm{Mpc}^{1.77}$, at the lower end of our cluster richness distribution, and $\sim$320 at $1000\ h_{50}^{-1}\ \mathrm{Mpc}^{1.77}$ for very rich clusters. (Note that these error bars are not identical to the detection significance for the cluster, but instead reflect the uncertainty in the measurement of the cluster's richness.) Convolving these relations predicts that the true distribution in richness for a measured $B_{gc,red}$ is skewed to lower values, with a mean value that is $\sim$80%–90% of the measured value. We then use our observed relationship between X-ray temperature derived from the CNOC clusters and B_{gc} to calculate that the mean observed temperature for RCS clusters should be about 10% lower than the expected relationship at $B_{gc,red} = 1000\ h_{50}^{-1}\ \mathrm{Mpc}^{1.77}$ and about 20% lower at $B_{gc,red} = 500\ h_{50}^{-1}\ \mathrm{Mpc}^{1.77}$. These decrements will also tend to steepen the logarithmic slope of the T_X-B_{gc} relationship by about 0.15. Varying the distribution parameters within reasonable limits produces corrections on the order of 10%–30% in normalization at a given $B_{gc,red}$ and a systematic increase of 0.1–0.3 in the slope. Comparison with the T_X-$B_{gc,red}$ relation shown in Figure 10 suggests that a correction for this Eddington bias would ameliorate the discrepancies between the RCS and CNOC samples, likely resulting in statistical agreement between their respective fits.

A similar calculation for X-ray luminosities was performed, with decrements in the X-ray luminosity of about 40% and 25% beneath predicted values at $B_{gc,red} = 500$ and $1000\ h_{50}^{-1}\ \mathrm{Mpc}^{1.77}$, respectively, steepening the logarithmic slope of the L_X-$B_{gc,red}$ relationship by about 0.3. This correction is not, however, sufficient to create agreement between the RCS and CNOC samples once bias in richness measurements has been accounted for, as is also indicated by their differing L_X-T_X relations. Note that these calculations assume that observational uncertainty is the primary source of scatter in the correlations.

A final consideration in comparing X-ray–selected and optically selected samples is the possibility that both selection methods produce biases when selecting clusters from a population with a significant intrinsic variation in X-ray or optical properties. If there is a significant intrinsic scatter in the properties of gas in cluster cores, systematic differences in X-ray characteristics between optically and X-ray–selected samples may naturally arise. The ROXS survey, a joint X-ray/optical survey for clusters (Donahue et al. 2002), found that some of their optically selected clusters had lower than expected L_X, suggesting that selection effects could be culpable. Gilbank et al. (2004) also

performed an independent X-ray/optical survey for clusters, using the red-sequence and the monochromatic matched-filter techniques. They found that the red-sequence methodology significantly outperforms monochromatic techniques in discovering and characterizing clusters. Even so, they also found a significant difference in the X-ray luminosities of X-ray–selected versus optically selected clusters, with several examples of spectroscopically confirmed low-L_X clusters. More recently Stanek et al. (2006) report that Malmquist bias may be responsible for a higher (by a factor of ~ 2) average L_X in X-ray flux-limited samples. These studies all suggest that for a given cluster mass or temperature there is a significant intrinsic scatter in X-ray luminosity or optical richness, or possibly both.

If this is the case, then both X-ray–selected and optically selected clusters may be prone to bias. We first consider the effects of such bias on our observed L_X-T_X relations, where we found the RCS clusters to be systematically lower in luminosity for a given temperature, and in addition calculate lower core gas fractions. This discrepancy could be interpreted as evidence for evolution in the properties of the ICM, and the loose agreement of the RCS data with the high-redshift X-ray–selected sample of Ettori et al. (2004a) supports this conclusion. In addition, our X-ray–luminous CNOC comparison sample may include a significant bias. These clusters were chosen from the wide-area EMSS (Gioia et al. 1990), primarily based on their X-ray luminosities, and may indeed represent a sample of particularly luminous clusters. We summarize by noting that these selection biases in both X-ray and optical samples can be significant, but they can be evaluated quantitatively, given additional independent information about the underlying cluster mass. In general, variations in the X-ray properties of clusters can be inferred most robustly from optically selected clusters, and vice versa, to minimize these effects.

10. SUMMARY AND DISCUSSION

We have performed an in-depth X-ray investigation of 13 high-redshift ($0.6 < z < 1.1$) optically selected clusters of galaxies from the RCS (Table 1). All but one of these clusters were detected by *Chandra* at an S/N of greater than 3 (Table 2), although two additional clusters in our sample (RCS 1417+5305 and RCS 2112−6326) did not possess enough signal to support further analysis. Initial imaging of the objects reveals that the RCS sample spans a wide range in cluster morphology (Fig. 1), from very regular objects (e.g., RCS 1419+5326) to more disturbed systems (e.g., RCS 2112−6326).

Surface brightness profiles were extracted for 10 clusters in $1''$–$2''$ annular bins and were reasonably well fitted by single β models (Fig. 2 and Table 3). Cluster emission was modeled with XSPEC, beginning with a spectral extraction region of 300 kpc radius. The results of single-temperature spectral fits, combined with best-fit β models, were used to determine R_{2500}. Spectra were reextracted from regions of that radius for further temperature fitting and R_{2500} luminosity estimates, until extraction regions and R_{2500} estimates were in agreement. Results of this process are given in Table 4. We have also used the σ-T_X relationship to compare the X-ray temperatures of three of our objects to currently available velocity dispersions (Gilbank et al. 2007, 2008). We find consistency in all cases (Table 6), suggesting that these three objects are at least relatively undisturbed.

Using the results of both spectral fitting and surface brightness modeling, X-ray masses were calculated for 10 clusters in our sample out to R_{2500} (Table 7), with extrapolation to R_{500} (Table 8). Canonical X-ray scaling laws were investigated for nine clusters

and compared to those of the moderate-redshift ($0.1 < z < 6$) CNOC sample (Tables 9 and 10). For the L_X-T_X relationship (Fig. 3), both RCS and CNOC fits have slopes consistent with self-similar predictions; however, their normalizations disagree. Interestingly, the slope of our combined RCS-CNOC sample agrees with that of X-ray–selected clusters at similar redshift (Ettori et al. 2004a), suggesting that evolution in the normalization of the L_X-T_X relationship may lie behind the observed steeper slopes. Results from L_X-M_{tot} fits are qualitatively very similar to those of the L_X-T_X relationship (Fig. 4); RCS and CNOC slopes are consistent with self-similarity at R_{2500} but disagree in normalization due to differing ICM densities.

The most notable outcome of our mass estimations is that the $\Delta = 2500$ gas mass fractions of RCS clusters are lower than expected by a factor of ~ 2 (Vikhlinin et al. 2006). Low gas mass fractions are also reported in the findings of other high-redshift cluster studies, both observation and theory (Lubin et al. 2002; Ettori et al. 2004b, 2006; Kravtsov et al. 2005; Sadat et al. 2005; Nagai et al. 2007; Afshordi et al. 2007). Physical explanations for low gas fractions include suggestions that much of the baryonic mass has been converted into stars, that the gaseous component of these clusters is still infalling, or that some mechanism (i.e., galaxy formation, AGNs, mergers, radio jets) is responsible for raising the entropy of the gas. Although we do see some evidence for higher entropy in the RCS sample (Fig. 7), it may not be enough to explain the entire f_{gas} discrepancy. Further study will have to be undertaken to determine whether the overall lower gas fractions that permeate this sample are ubiquitous at high redshift or an outcome of sample selection.

Explanations aside, the growing evidence that massive ($T_X \sim 6$ keV) clusters may have an evolving or broad range of central gas mass fractions may have important consequences for the interpretation of future cluster surveys in the microwave and X-ray bands, which select in part on the basis of central gas density. Scatter in this parameter will tend to reduce completeness and, if not properly accounted for, inject bias in the cluster samples such surveys produce. In addition, since SZ mass determinations tend to rely on the assumption of a constant gas mass fraction (Reid & Spergel 2006), complementary data may be required to avoid systematic errors in SZ total mass estimates.

Using red-sequence optical richness measurements of both samples, the relationships between $B_{gc,red}$ and global cluster properties (T_X, L_X, M_{2500}, and M_{200}) were investigated (Table 11). We find that $B_{gc,red}$ is poorly correlated to X-ray luminosity, with average scatter in the relationships reaching $\sigma_{\log Y} \sim 0.36$. Temperature, however, is nicely predicted by optical richness, showing scatter comparable to that obtained by using L_X, although this measurement may exclude several of the strongest outliers in our sample. Richness-mass relationships are generally consistent with one another and with previous studies (Yee & Ellingson 2003; Blindert et al. 2007), and we find an average scatter of $\sigma_{\log Y} \sim 0.30$ for these relationships (Fig. 11). Although this scatter is on average somewhat higher than the other mass proxies investigated here (by 0.07–0.19 in $\sigma_{\log Y}$), the comparative speed and ease with which it can be obtained still recommend it as a promising tool for mass estimations of large high-redshift cluster samples.

REFERENCES

Afshordi, N., Lin, Y., Nagain, D., & Sanderson, A. J. R. 2007, MNRAS, 378, 293
Akritas, M. G., & Bershady, M. A. 1996, ApJ, 470, 706
Allen, S. W., & Fabian, A. C. 1998, MNRAS, 297, L57
Allen, S. W., Schmidt, R. W., & Fabian, A. C. 2001, MNRAS, 328, L37
Arnaud, K. A. 1996, in ASP Conf. Ser. 101, Astronomical Data Analysis Software and Systems V, ed. G. H. Jacoby & J. Barnes (San Francisco: ASP), 17
Arnaud, M., & Evrard, A. E. 1999, MNRAS, 305, 631
Arnaud, M., Pointecouteau, E., & Pratt, G. W. 2005, A&A, 441, 893
———. 2007, A&A, 474, L37
Bauer, F. E., et al. 2002, AJ, 123, 1163
Blindert, K., Yee, H. K. C., Ellingson, E., Gladders, M. D., Gilbank, D. G., Barrientos, L. F., & Golding, J. 2007, ApJS, submitted
Borgani, S., et al. 2004, MNRAS, 348, 1078
Bower, R. G., Bohringer, H., Briel, U. G., Ellis, R. S., Castander, F. J., & Couch, W. J. 1994, MNRAS, 268, 345
Cain, B., et al. 2008, ApJ, 679, 293
Cohn, J. D., Evrard, A. E., White, M., Croton, D., & Ellingson, E. 2007, MNRAS, 382, 1738
Dell'Antonio, I. P., Geller, M. J., & Fabricant, D. G. 1995, AJ, 110, 502
Dickey, J. M., & Lockman, F. J. 1990, ARA&A, 28, 215
Donahue, M., et al. 2002, ApJ, 569, 689
Eastman, J., Martini, P., Sivakoff, G., Kelson, D. D., Mulchaey, J. S., & Tran, K. 2007, ApJ, 664, L9
Edge, A., & Stewart, G. 1991, MNRAS, 252, 428
Ettori, S. 2000, MNRAS, 311, 313
Ettori, S., Dolag, K., Borgani, S., & Murante, G. 2006, MNRAS, 365, 1021
Ettori, S., Tozzi, P., Borgani, S., & Rosati, P. 2004a, A&A, 417, 13
Ettori, S., Tozzi, P., & Rosati, P. 2003, A&A, 398, 879
Ettori, S., et al. 2004b, MNRAS, 354, 111
Finoguenov, A., Reiprich, T. H., & Bohringer, H. 2001, A&A, 368, 749
Gilbank, D. G., Yee, H. K. C., Ellingson, E., Gladders, M. D., Barrientos, L. F., & Blindert, K. 2007, AJ, 134, 282
Gilbank, D. G., Yee, H. K. C., Ellingson, E., Hicks, A. K., Gladders, M. D., Barrientos, L. F., & Keeney, B. 2008, ApJ, 677, L89
Gilbank, D. G., et al. 2004, MNRAS, 348, 551
Gioia, I. M., Henry, J. P., Maccacaro, T., Morris, S. L., Stocke, J. T., & Wolter, A. 1990, ApJ, 356, L35
Gladders, M. D. 2002, Ph.D. thesis, Univ. Toronto
Gladders, M. D., & Yee, H. K. C. 2000, AJ, 120, 2148
———. 2005, ApJS, 157, 1

Hicks, A. K., Ellingson, E., Yee, H. K. C., & Hoekstra, H. 2006, ApJ, 652, 232
Hicks, A. K., et al. 2007, ApJ, 671, 1446
Kotov, O., & Vikhlinin, A. 2005, ApJ, 633, 781
Kravtsov, A. V., Nagai, D., & Vikhlinin, A. 2005, ApJ, 625, 588
Kravtsov, A. V., Vikhlinin, A., & Nagai, D. 2006, ApJ, 650, 128
Lacey, C., & Cole, S. 1993, MNRAS, 262, 627
Longair, M. S., & Seldner, M. 1979, MNRAS, 189, 433
Lubin, L. M., Oke, J. B., & Postman, M. 2002, AJ, 124, 1905
Markevitch, M. 1998, ApJ, 504, 27
Maughan, B. J. 2007, ApJ, 668, 772
Nagai, D., Kravtsov, A. V., & Vikhlinin, A. 2007, ApJ, 668, 1
Nulsen, P. E. J., Hambrick, D. C., McNamara, B. R., Rafferty, D., Birzan, L., Wise, M. W., & David, L. P. 2005, ApJ, 625, L9
Ponman, T. J., Cannon, D. B., & Navarro, J. F. 1999, Nature, 397, 135
Ponman, T. J., Sanderson, A. J. R., & Finoguenov, A. 2003, MNRAS, 343, 331
Popesso, P., Biviano, A., Bohringer, H., & Romaniello, M. 2007, A&A, 461, 397
Postman, M., et al. 1996, AJ, 111, 615
Reid, B. A., & Spergel, D. N. 2006, ApJ, 651, 643
Sadat, R., et al. 2005, A&A, 437, 31
Sanderson, A. J. R., Ponman, T. J., Finoguenov, A., Lloyd-Davies, E. J., & Markevitch, M. 2003, MNRAS, 340, 989
Sarazin, C. L. 1988, X-Ray Emissions from Clusters of Galaxies (Cambridge: Cambridge Univ. Press)
Spergel, D. N., et al. 2007, ApJS, 170, 377
Stanek, R., Evrard, A. E., Böhringer, H., Schuecker, P., & Nord, B. 2006, ApJ, 648, 956
Valtchanov, I., et al. 2004, A&A, 423, 75
Vikhlinin, A., Kravtsov, A., Forman, W., Jones, C., Markevitch, M., Murray, S. S., & Van Speybroeck, L. 2006, ApJ, 640, 691
Voit, G. M. 2005, Rev. Mod. Phys., 77, 207
White, D. A., Jones, C., & Forman, W. 1997, MNRAS, 292, 419
Wilkes, B., Green, P., Cameron, R., Evans, N., Ghosh, H., Kim, D. W., & Tananbaum, H. 2000, AAS High Energy Astrophys., 32, 1212
Xue, Y., & Wu, X. 2000, ApJ, 538, 65
Yee, H. K. C., & Ellingson, E. 2003, ApJ, 585, 215
Yee, H. K. C., Ellingson, E., & Carlberg, R. G. 1996, ApJS, 102, 269
Yee, H. K. C., Gladders, M. D., Gilbank, D. G., Majumdar, S., Hoekstra, H., & Ellingson, E. 2007, in ASP Conf. Ser. 379, Cosmic Frontiers, ed. N. Metcalfe & T. Shanks (San Francisco: ASP), 103
Yee, H. K. C., & Lopez-Cruz, O. 1999, AJ, 117, 1985